IEEE Access
Multidisciplinary ┊ Rapid Review ┊ Open Access Journal

Enabling Multi-Functional 5G and Beyond User Equipment: A Survey and Tutorial

YIMING HUO[1], **(Member, IEEE), XIAODAI DONG**[1], **(Senior Member, IEEE),**
WEI XU[2], **(Senior Member, IEEE), AND MARVIN YUEN**[3], **(Member, IEEE)**
[1]Department of Electrical and Computer Engineering, University of Victoria, Victoria, BC V8P 5C2, Canada
[2]National Mobile Communications Research Laboratory (NCRL), Southeast University, Nanjing 210096, China
[3]Kingston Technology, Fountain Valley, CA 92708, USA

Corresponding author: Yiming Huo (ymhuo@uvic.ca)

ABSTRACT The fifth generation (5G) research and development has been fueled by many new breakthroughs in various areas. The recent progress in carrier aggregation (CA), licensed assisted access (LAA), massive MIMO (MaMi), beamforming techniques, cooperative spectrum sensing (CSS), compressive sensing (CS), machine learning, etc., has provided inspiring and promising approaches to address 5G and beyond challenges. However, at the user equipment (UE) end, limited design budget and hardware resources bring along a series of challenging implementation issues when delivering multi-standard and multi-functional wireless communications. In this paper, we first review recent advances in technical standards and critical enabling techniques, accompanied with several case studies of product developments. After the classification of typical 5G application and deployment scenarios, we propose and analyze a novel hardware reuse and multiplexing solution to facilitate cost-effective and energy-efficient UE design, followed by an investigation of state-of-the-art hardware development from the systems and circuits standpoint. Moreover, wireless UE hardware solutions, UE proof-of-concept (PoC) implementation and field test are proposed and discussed. Finally, the new trends of UE design and terahertz technologies for 5G and beyond applications are investigated and envisioned.

INDEX TERMS 5G, user equipment, millimeter wave (mmWave), beamforming, massive MIMO (MaMi), beam management, distributed phased arrays MIMO (DPA-MIMO), carrier aggregation (CA), licensed-assisted access (LAA), machine learning, deep learning, terahertz (THz), 6G, smartphone.

NOMENCLATURE

3GPP	Third Generation Partnership Project (3GPP)
5G	Fifth Generation
6G	Sixth Generation
ADC	Analog-to-Digital Converter
AI	Artificial Intelligence
ASM	Antenna Switching Module
BB	Baseband
BF	Beamforming
BFM	Beamforming Module
BS	Base Station
CA	Carrier Aggregation
CC	Carrier Component
CMOS	Complementary Metal-Oxide-Semiconductor
CS	Compressive Sensing
CSI	Channel State Information
CSS	Cooperative Spectrum Sensing
DAC	Digital-to-Analog Converter
DC	Direct Current
DPA-MIMO	Distributed Phased Arrays Based MIMO
ECC	Envelope Correlation Coefficient
EIRP	Effective Isotropic Radiated Power
FCC	Federal Communications Commission
FDD	Frequency Division Duplex
FoM	Figure of Merit
FinFET	Fin Field Effect Transistor
GNSS	Global Navigation Satellite System
ILFM	Injection-locked Frequency Multiplier
IoT	Internet of Things
LAA	Licensed Assisted Access
LBT	Listen Before Talk

The associate editor coordinating the review of this article and approving it for publication was Zhenyu Xiao.

LNA	Low Noise Amplifier
LoS	Line-of-Sight
LO	Local Oscillator
LWA	LTE-WLAN Aggregation
MAC	Medium Access Control
MaMi	Massive MIMO
MIMO	Multiple-Input-Multiple-Output
MLB	Main Logic Board
mmWave	Millimeter-Wave
MMIC	Monolithic Microwave Integrated Circuit
NLoS	Non-Line-of-Sight
NOMA	Non-Orthogonal Multiple Access
NR	New Radio
PA	Power Amplifier
PAPR	Peak-to-Average Power Ratio
PCB	Printed-Circuit Board
PHY	Physical Layer
PLL	Phase-locked Loop
PMU	Power Management Unit
PoC	Proof of Concept
PULT	Peak Uplink Throughput
QAM	Quadrature Amplitude Modulation
QoE	Quality of Experience
QoS	Quality of Service
RF	Radio Frequency
RX	Receiver
SE	Spectral Efficiency
SiGe	Silicon-Germanium
SM	Spatial Multiplexing
SNR	Signal-to-Noise Ratio
SoC	System-on-Chip
SOI	Silicon On Insulator
SPDT	Single Pole Double Throw
TDD	Time Division Duplex
THz	Terahertz
TX	Transmitter
UAV	Unmanned Aerial Vehicle
UE	User Equipment
UV	Ultraviolet
VCO	Voltage Controlled Oscillator
WiGig	Wireless Gigabit Alliance
WLAN	Wirless Local Area Network
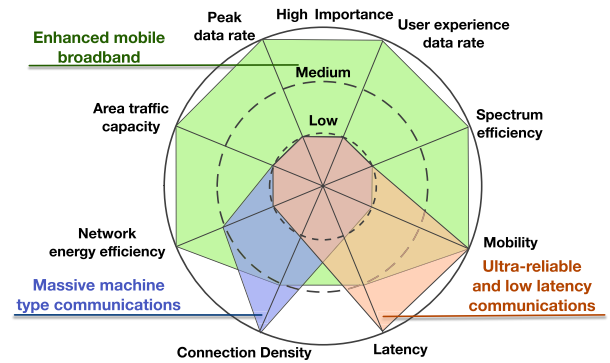
FIGURE 1. Three principle 5G usage scenarios in ITU model [1].

I. INTRODUCTION

Today, the research and development (R&D) of 5G technologies advance with unprecedented proliferation and serves as the catalyst of accelerating the global 5G deployment. In September 2015, the International Telecommunication Union (ITU) defined three principle usage scenarios for 5G: Enhanced Mobile Broadband (eMBB), Ultra Reliable Low Latency Communications (uRLLC), and Massive Machine Type Communications (mMTC) [1]. The representative service of uRLLC implies a very high importance on low latency with high mobility and security. A typical requirement of control plane latency and reliability is 1 ms and 99.999%
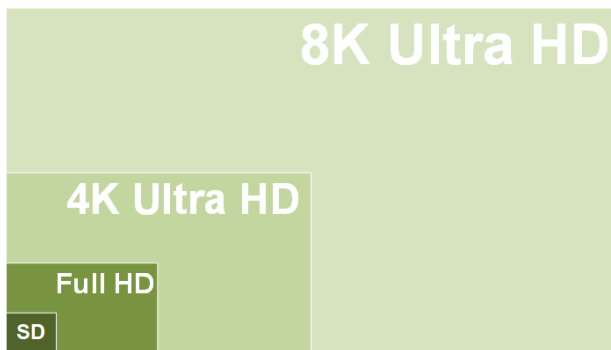
reliability, respectively. Its applications and usage can be found in areas, such as, autonomous vehicles that have high safety dependency on reliability and latency [2], [3]; Industry 4.0 [4] which facilitates the wireless control of industrial manufacturing; e-Health such as remote medical care and surgery [5], rescue support robot, public security, aviation, and other mission critical applications.

On the other hand, the mMTC service enables energy-efficiency sensitive applications; smart city can be seen as a typical usage scenario, with a typical connection density over 1,000,000 devices/km^2. Mobile edge computing (MEC) [6] and converged cell-less communications schemes co-enable a better quality of service (QoS) in smart cities [7]. Furthermore, since mMTC service necessitates ultra-densely deployed BSs to support massive number of users, it can lead to prohibitively large overheads, unaffordable complexity, and high cost and/or power consumption due to the large number of samples required by the Nyquist sampling theorem [8]. Therefore, the compressive sensing (CS) technique that provides a sub-Nyquist sampling approach can significantly reduce the data volume generated by each device for mMTC communications. Moreover, Ke *et al.* proposed a CS based adaptive active user detection (AUD) and channel estimate scheme in [9] that can address the reliable massive access problem of massive connectivity via adjusting the time slot overhead.

Mainly addressing the human-centric use cases, e.g., human-to-human (H2H) communications, eMBB is expected to achieve a high comprehensive performance in eight key indexes of 5G use scenarios as illustrated in Fig. 1. EMBB needs to excel in six key indexes and obtain at least medium performance in the other two; compared to uRLLC and mMTC, either of which requires a full score in only one or two key indexes. Moreover, in terms of the guidelines for evaluating the radio interface technologies for IMT-2020, three of five connectivity scenarios are assigned to eMBB: Indoor Hotspot (IH), Dense Urban (DU), and Rural (RU). Therefore, eMBB may play an essential role among the three major dimensions of 5G use scenarios. 5G eMBB is expected to enable high quality video/audio streaming, e.g., 4K ultra high definition (UHD), 8K UHD

FIGURE 2. Video resolution scaling up.

FIGURE 3. Conceptual illustration of smartphone with holographic display.

(7680 pixels × 4320 lines), 3D UHD, immersive entertainment (virtual reality and mixed reality) and even hologram video calls [10] as shown in Figs. 2–3. On the other hand, 5G eMBB can be extended from conventional terrestrial communications to aerial communications, e.g., unmanned aerial vehicle (UAV) cellular mmWave communications [11], [12].

With respect to designing the 5G new radio (NR) to deliver the aforementioned 5G services, a significant challenge is how to efficiently utilize the available resources, such as spectrum and hardware that are available currently or in the near future. Exploring additional spectrum more efficiently for cellular communications has not stopped since the 1G era, and in recent years, potential cellular bands located at 3-6 GHz or higher are being extensively investigated. In Fig. 4, cellular frequency bands (including unlicensed bands) used and reserved in major countries are plotted. Moreover, channel models up to 100 GHz have been thoroughly studied in [7], followed by the Federal Communications Commission (FCC)'s decision to adopt new Upper Microwave Flexible Use Service [13]. Proof-of-concept (PoC) or prototyping designs of devices and systems based on high millimeter wave (mmWave) bands (>100 GHz) and terahertz (THz) spectrum have been investigated in [14]–[20], which lays the foundation for potential 5G and beyond, or 6G applications, although there are many challenges to overcome.

Carrier aggregation (CA) emerges as a cost-effective technique to overcome the spectrum fragmentation issue [21] and the Release 13 of the Third Generation Partnership Project (3GPP Rel. 13) can support up to 32 carrier components (CCs). In the near future, more complicated 5G CA, will be applied beyond 6 GHz.

Another solution to alleviate spectrum scarcity is to apply the shared spectrum paradigms. LTE in unlicensed spectrum (LTE-Unlicensed) has been proposed to allow cellular network operators to access the unlicensed frequency band to offload data traffic. The first version of LTE-Unlicensed is known as LTE-U developed by the LTE-U Forum. However, LTE-U is not a global standard because it only utilizes the carrier-sensing adaptive transmission (CSAT) scheme, and does not mandate the listen-before-talk (LBT) technique that is required in Japan and EU. In 2015, Google expressed the concern of LTE-U's lack of an effective coexistence mechanism when WiFi is received at a power level below −62 dBm [22]. Therefore, the second variant of LTE-Unlicensed, licensed-assisted access (LAA), which integrates both CSAT and LBT functions, is standardized in 3GPP Rel. 13. Moreover, both uplink and downlink features have been introduced in enhanced licensed-assisted access (eLAA) of 3GPP Rel. 14. As new bands, e.g., mmWave bands, will be exploited for future 5G networks, more flexible but complicated ''5G-LAA'' CA combinations need to be investigated. Moreover, 5G NR ultra dense networks need more advanced protocols, such as cooperative LBT to reduce the collision probability [23], pairLBT technique that improves the ability to perform carrier sense by avoiding hidden node issues [24] and so on.

Compared to LTE-U and LAA which require hardware changes (for both infrastructure and hand-held devices) for unlicensed LTE transmission to coexist with WiFi signals, LTE-Wirless Local Area Network (WLAN) aggregation (LWA) can enable configuration of inter-networking to utilize both networks simultaneously, and allows mobile network operator (MNO) to deliver the service with well-established networks and access points [25]. As observed from Table 1 [25], LWA outperforms LAA, in terms of additional UE cost and cellular infrastructure impact. Considering that enhanced LWA (eLWA) has been scheduled in 3GPP Rel. 14 to introduce and support Wireless Gigabit Alliance (WiGig) 60 GHz band, eLWA may obtain more performance gains compared to the current LAA. However, a later version of LAA is also envisioned to include WiGig bands. Therefore, in this paper, 5G-LAA is one of our main focuses and it will be thoroughly investigated and analyzed. Since 5G-LAA, compared to eLWA, may bring more UE design challenges at both the physical layer (PHY) and the medium access control (MAC) layer, we will mainly deal with LAA design, instead of LWA.

Massive-MIMO (MaMi), Multi-user MIMO (MU-MIMO), distributed phased array MIMO (DPA-MIMO) [26], non-orthogonal multiple access (NOMA), and other new multiple antenna/multiple access techniques, can be seen as

TABLE 1. Comparison of LAA and LWA [25].

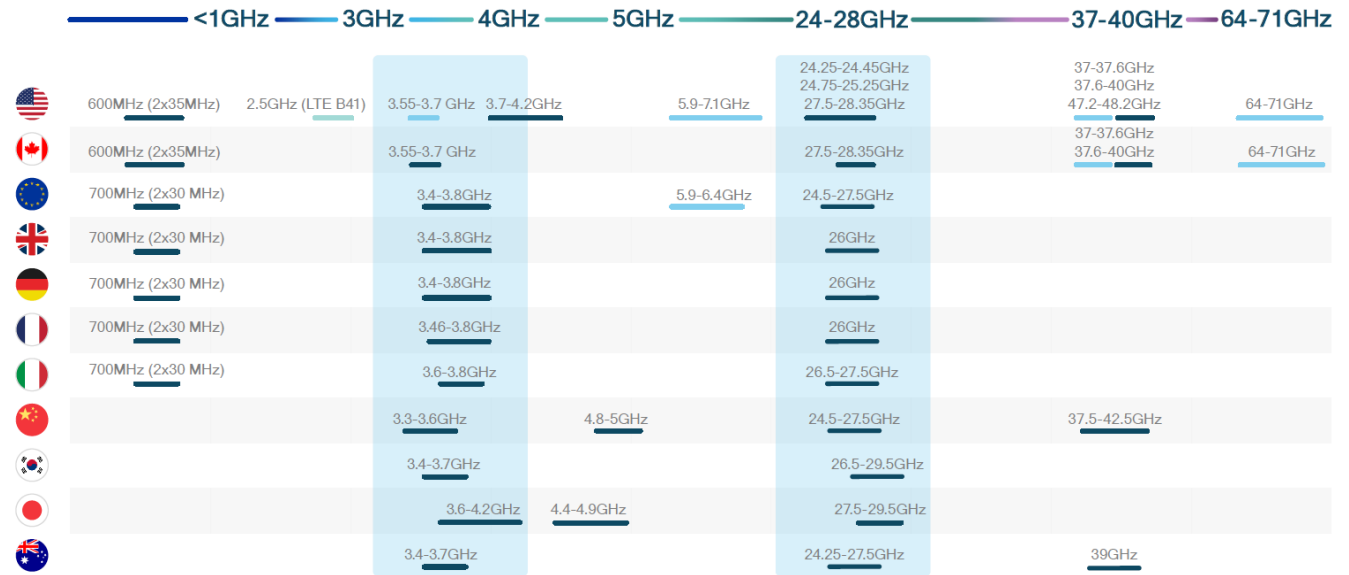| Technology	Performance Gain	WLAN Infrastructure Impact	Cellular Infrastructure Impact	Additional UE Cost	Same Network For LTE & WLAN Users
LAA	High	N/A	High	Medium	No
LWA	High	Medium	Medium	Low	Yes

FIGURE 4. Global spectrum occupation by regions [29].

alternative means to increase capacity when the spectrum resource becomes a major constraint. In particular, NOMA can efficiently utilize the limited spectrum resources to support multiple users in the same time/frequency resource block and distinguishes them in power domain or code domain [27]. User fairness in mmWave NOMA with analog beamforming is studied in [28] with a solution achieving near upper-bound performance.

Because 5G NR systems must support multiple wireless standards occupying a plethora of frequency bands and advanced technologies for various functions, the implementation challenge is technically and commercially unprecedented. This paper focuses on the system and hardware perspectives for 5G NR implementation. From the base station (BS) end, adopting more bands, particularly the mmWave bands, can drastically increase the complexity, cost, bulk, and power consumption. To support a wide range of modulation and multiple access technologies, the 5G modem design becomes more complicated than ever using significantly more hardware and software resources. But a more serious challenge is at the user equipment (UE) end, which stems from several design constraints including but not limited to, battery lifetime, overall product design, user experience, and reliability. For example, existing wireless user equipment can only accommodate a limited number of MIMO antennas and wireless chipsets without compromising

the overall product design and user experience [26]. In order to maintain a satisfactory UE figure-of-merit (FoM) defined in [26], judiciously arranging and utilizing the hardware resources in the UE design is highly relevant. In this paper, we carry out a study of dominant and potential enabling technologies and design techniques of 5G and beyond user equipment. Furthermore, we propose and evaluate cost-effective solutions for energy-efficient, multi-function, multi-standard, wireless UE designs.

The remainder of this paper is arranged as follows. Section II conducts an investigation of current mainstream carrier aggregation techniques, spectrum sharing paradigms and the related implementation challenges. In Section III, we first present the review and comparison of promising 5G wireless technologies that are categorized based on application and deployment scenarios, and then unveil the critical design constraints on the physical layer. Section IV proposes a novel system architecture facilitating efficient mode switching between cellular and WiFi for various application scenarios. Furthermore, Section V evaluates the most advanced 5G and WiFi mmWave hardware designs for antennas, systems and circuits and makes the prediction of future requirements in these areas. Section VI presents the critical wireless and product co-design methodology and examples, plus a specific proof-of-concept UE design with field test results. Some new and future trends such as foldable UE design and THz
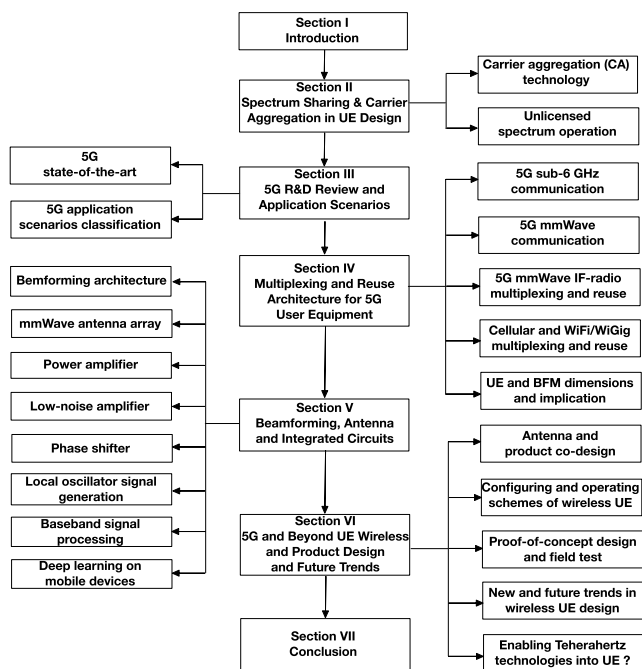
FIGURE 5. The overall organization of this paper.

technologies are reviewed and discussed. Finally, Section VII concludes this survey paper. In order to clearly explain the logic flow of these sections, Fig. 5 presents the overall architecture of this paper in a diagram.

II. SPECTRUM SHARING AND CARRIER AGGREGATION IN UE DESIGN

The radio spectrum for civil applications is increasingly crowded. By giving a full frequency scan through MHz to THz, as redrawn based on a spectrum map in [29], more and more bands have been and will be added into both licensed and unlicensed spectrum.

Among the released bands in 3GPP Rel. 13 and its later versions, Band 72 targets 450 MHz Narrowband IoT (NB-IoT), Bands 252 and 255 are solely for LTE-Unlicensed and restricted to Evolved Universal Terrestrial Radio Access (E-UTRA) operation when carrier aggregation is configured, Band 46 serves LTE-Unlicensed Time Division Duplex (TDD) band, and Band 47 is a TDD Vehicle-to-Everything (V2X) band that occupies 70 MHz bandwidth. It is worth mentioning that LTE-V2X has a frequency overlap, from 5855 MHz to 5925 MHz due to an IEEE 802.11p amendment which is also known as Wireless Access in Vehicular Environments (WAVE). However, LTE-V2X outperforms IEEE 802.11p in terms of reliability and mobility [30].

Furthermore, several licensed high bands are proposed for 5G NR frequency range 2 (FR2), e.g., 24.25–27.5 GHz, 27.5–29.5 GHz, 37–40 GHz. Moreover, several sub-6 GHz bands are used for 5G NR mid bands such as 3400-3800 MHz and 4400–4900 MHz. Compared to 5G NR high bands, 5G NR mid bands hold richer multipath propagation and

better scattering natures; accordingly, it enables higher spatial multiplexing gain (SMG), which makes 5G low bands more suitable for Macro cells required for high user mobility and massive MIMO applications.

A. CARRIER AGGREGATION

As summarized in [31], there are a total of 900 CA combinations regulated. Downlink CA combinations compose of both regular LTE band groups and LTE-LAA ones, for example, LB/LB/MB/MB/HB (LB: LTE low band; MB: LTE mid band; HB: LTE high band), and HB/LAA/LAA/LAA/LAA (LAA: Band 46). However, as for enabling more CCs, for example, up to the 32 specified in 3GPP Rel. 13, the overwhelming challenge lies in the high performance hardware needed and the extreme requirements for hardware resources and energy efficiency.

In light of CA categorization, there are contiguous intra-band CA, non-contiguous intra-band CA, and inter-band CA. Inter-band CA is the most challenging, with the most resources used. Take an inter-band downlink 3CCs CA, for example B2/B5/B30; the block diagram of hardware circuit and system is depicted in Fig. 6. Starting from the primary multi-band antenna (operating from 600 to 2700 MHz), a pentaplexer divides the signal into five bands: LTE-low band, LTE mid band, LTE-high band, Wi-Fi/Bluetooth, and global navigation satellite system (GNSS). For cellular bands, antenna switch modules (ASMs) further execute band selection. After being processed by duplexers, PAs, and LNAs, the task by the RF front end is accomplished and 4G transceivers take over the job from then on. As mentioned, inter-band CA has to use an individual ASM, duplexer, power amplifier (PA), low-noise amplifier (LNA), and corresponding transceiver, which implies that it is more complicated and resource-consuming than its contiguous intra-band CA counterpart. Moreover, enabling inter-band MIMO with a larger number of CCs could be more resource-intensive. Consequently, the quantity of antennas, front ends and transceivers will have to be scaled up.

Besides the aforementioned challenges in resource requirements, another major technical issue is known as RF 'desense' (degradation of sensitivity) that happens mainly due to insufficient isolation from either the antenna level, devices (chipsets) level, board design level [26], [32], or a more comprehensive system level [33]. It is envisioned that at 5G UE end, the RF desense issue is more exacerbated and complicated.

B. UNLICENSED SPECTRUM OPERATION

Considering the unlicensed spectrum used by wireless UE, currently there are 915 MHz ISM bands for ZigBee, Z-wave applications; 2412-2484 MHz for 2.4 GHz WLAN applications (IEEE 802.11b/g/n/ac); 5150-5850 MHz for 5 GHz WLAN applications (IEEE 802.11a/h/j/n/ac); 5850-5925 MHz for IEEE 802.11p; 57-71 GHz (in U.S. [13]) for WiGig IEEE 802.11ad. What follows is IEEE 802.11ax that may add additional bands between 1 to 6 GHz [35].
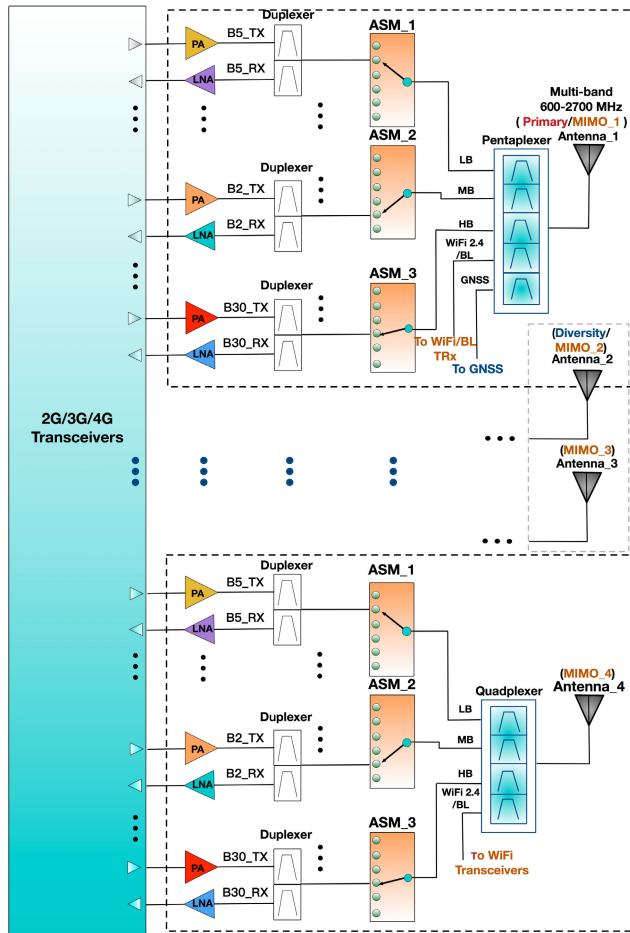
FIGURE 6. Carrier aggregation 4G front-end example.

FIGURE 7. (a) Contemporary building (University of Victoria McPherson Library) with massive tinted glass, (b) 5G modem solution by Verizon and Nokia Bell Labs [41].

As the successor of IEEE 802.11ad, 802.11ay can deliver enhanced performance by enabling wider bonded channels (more than 4 times the bandwidth of 802.11ad) and higher orders of modulation and MIMO.

Today, some of the unlicensed bands have already been assigned to the 3GPP "shared" spectrum to coexist with LTE bands, e.g., bands 46, 252, 255, for LAA usage. Furthermore, as envisioned, some unlicensed frequency bands higher than 6 GHz, such as 57-71 GHz, will be soon labeled as the shared spectrum, in order to enable cooperation with 5G mmWave high bands. Likewise, 5G-LAA bands can be expanded to 57-71 GHz and therefore 5G-LAA CA combinations can be more diverse and complicated. In an extreme example, we can obtain a powerful CA combination defined as "Super-CA" that was proposed in [34]. Super-CA combines both LTE-LAA and 5G-LAA techniques, and copes with a wider spectral range from sub-6 GHz upto 95 GHz (or even higher) that is composed of future cellular and WiFi mmWave frequencies.

For example, a 5-CCs-based Super-CA combination can be denoted as B2/B5/B30/5G-28/5G-39, where 5G-28 and 5G-39 stand for 5G 28 GHz and 39 GHz bands respectively. Another exemplary case is B40/B46/5G-28/5G-39/5G-LAA, where 5G-LAA can be the 5G unlicensed band in the current
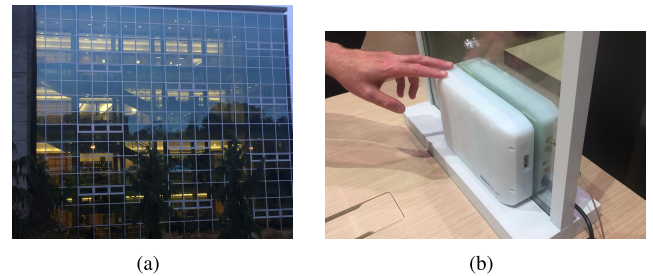
57-71 GHz frequency range or any other unlicensed mmWave bands, particularly for 5G shared spectrum usage in the near future.

Assume that a cellular operator owns multiple 200 MHz sub-bands out of 5G high bands, a 5-CCs-based 5G Super-CA combination, such as B40/B46/5G-28/5G-39/5G-LAA, can enable a total RF bandwidth of 800 MHz, thus achieving significant wireless data throughput. If a larger number (> 5) of CCs or MIMO is used, the data rate can be higher.

However, implementing such a Super-CA at both BS and UE ends is enormously challenging. First, multiple RF front-end chipsets operating at 3/4G's sub-6 GHz and 5G mmWave high bands, are necessary. In the RF front end of 4G UE, there are power amplifiers (PAs), ASMs, diplexers, duplexers, multiplexers, etc., which are compatible to LTE standards, while in a 5G Super-CA case, more front-end blocks serving 5G low/mid/high bands (mmWave) need to be integrated and enabled. These front-end components are the major functional blocks determining the overall RF performance.

The foreseeable drastic increase in hardware complexity will lead to technical and commercial difficulties for 5G system design, particularly the UE design. Moreover, a slim form factor is mandatory and usually treated as high priority for 5G hand-held devices [26]. Consequently, it is impractical to compromise UE portability for higher wireless data throughput, from a real-life marketing standpoint. Furthermore, due to fabrication and testing complexity of 5G UE, the cost of both design and manufacture will be substantially high at the beginning. For example, the manufacture re-innovations may cause comparatively low yield until the quality control becomes more stable. Therefore, in the 5G era, the supply chain will scale up significantly [36] and become more diverse, while more challenging to manage than in the 4G era.

III. 5G R&D REVIEW AND APPLICATION SCENARIOS
A. 5G STATE-OF-THE-ART
Integrating more types of cutting-edge wireless technologies into future 5G wireless UE is an unswerving trend. The opportunity is self-evident in that as the wireless data throughput can be dramatically increased with lower latency, which enables and enriches many potential application scenarios, and improves the quality of user experience.

On the other hand, the available hardware resources at the UE end are limited and constrained by the state-of-the-art design and fabrication techniques [26]; in this regard, the future 5G wireless UE needs to provide not only the most advanced 5G cellular services, but also backward compatibility to legacy 3GPP standards and other wireless technologies.

Additionally, usage scenarios become more complicated than ever, and it is urgent to investigate and develop new MAC-layer protocols for cost-effectively operating UE in heterogeneous networks (HetNet). For example, such protocols need to determine when, where and how to enable or cooperate one or more wireless technologies, in terms of specific application scenarios; in this respect, application requirements, usage environments, user habits, local (region) policies, business modes, infrastructure availability, network stability, security, etc., will be taken into account when developing such protocols. In some country/region where mmWave networks and infrastructure are more practical and cost-efficient, 5G UE with mmWave communication functions may expect rational investment returns. Likewise, for places where customers tend to use high-speed WiFi services, 5G UE supporting IEEE 802.11ad/ay and voice-over-WiFi (VoWiFi) will be a more viable product.

5G mmWave for outdoor/indoor services is confronted with several challenges, one of which is related to the high penetration/absorption loss which has been well studied through experiments over different frequencies in [37]–[40]. The penetration loss has shown very strong dependency on materials and frequency. For example, [39] shows that concrete attenuation loss is 4.38 dB/cm at 45 GHz (H-H polarization); according to [40], at 73 GHz, for steel door, co-polarized penetration loss is as high as 9.9 dB/cm, whereas plasterboard wall (drywall) demonstrates a comparatively low co-polarized penetration loss of 0.8 dB/cm. These findings indicate the complexity and difficulty of 5G deployment.

In particular, buildings made of the concrete/brick and installed with the tinted glass energy-saving windows (Fig. 7(a)), have a relatively high cost of 5G mmWave infrastructure (e.g. femtocells) deployment. For example, Verizon and its partner Nokia Bell Labs have proposed a 5G modem solution to enable 5G mmWave signal transmission through ultraviolet (UV) rays blocking windows [41], as illustrated in Fig. 7(b). In addition, Verizon has demonstrated fixed wireless access (FWA) solutions for 5G residential broadband services over 5G new bands, with several outdoor and indoor infrastructures presented in Fig. 8.

However, as illustrated in Fig. 7(b) and Fig. 8(b), installing such a device attached to the window may have issues associated with expense, reliability, building aesthetics, endurance, maintenance, user experience, etc. On the other hand, a conventional gateway router (home unit) supporting existing Fiber Optic Service (FiOS) or Fiber-to-the-Building (FTTB) can be an alternative solution to enhance the indoor 5G wireless user experience. This also implies that WiGig can be an appealing and complementary solution for indoor

FIGURE 8. (a) Verizon 5G infrastructure (smallcell) on roof, and (b) Samsung home unit (femtocell) attached on window [42].
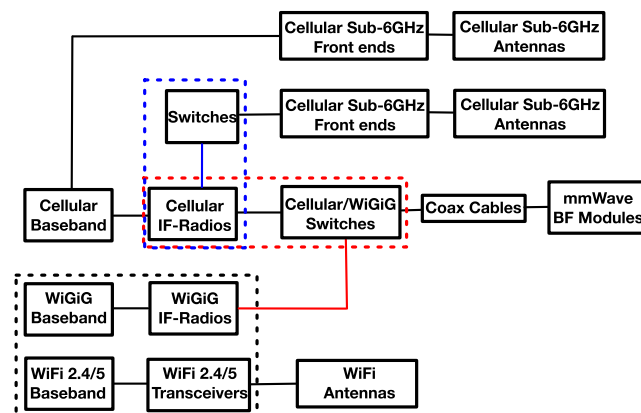

FIGURE 9. Block diagram of 5G cellular and WiFi (WiGig) multiplexing/reuse architecture [34].

short-range massive data communication over mmWave bands. To summarize, 5G UE designs will be more diversified, highly flexible and customized than its 4G counterpart.

B. 5G APPLICATION SCENARIOS CLASSIFICATION

Application scenarios in which both sub-6 GHz and above-6 GHz bands (28, 37, 39, 60, 64-71 GHz) are available for 5G cellular and WiFi networks, can be categorized into several representative types, in terms of inherent features, availability, and usage scenarios of these bands, as shown in Table 2. For transmission distance, coverage, infrastructure maturity and cost, UE application challenges are examined correspondingly. Table 2 obtains an overall and brief understanding of how to efficiently cope with different 5G application scenarios, thus designing both 5G MAC protocols and PHY hardware architecture effectively.

As observed from Table 2, each technology type has its corresponding typical application focus. Consequently, it is critical to implement and manage all these technologies in order to obtain the optimum performance gain for different application scenarios. Moreover, due to the practical UE design constraints aforementioned, cost-effective UE hardware architecture and PHY-MAC co-design need to be considered.

IV. MULTIPLEXING AND REUSE ARCHITECTURE FOR 5G USER EQUIPMENT

As more and more wireless technologies and hardware modules will be included in a single UE, cost and space

TABLE 2. Classification of wireless communication technologies used for 5G.

Technology Type	Spectrum Availability	Application Scenarios	Coverage & Penetrability	Distance & Mobility	Infrastructure Readiness & Cost	UE Application Challenge
1. 5G Sub-6 GHz (stand alone)	Widely distributed from 450 MHz to 6 GHz	High data rate; MaMi; 5G mmWave bands unavailable; Both urban and rural areas;	Wide, Strong (<5 GHz) and Medium (>5 GHz)	Long/ medium, high	High maturity for normal MU-MIMO applications; PoC stage for MaMi BS [44]- [46]; High cost for MaMi;	Large dimension of sub-6 GHz MaMi antennas; More hardware resources, high complexity and power consumption, for MaMi;
2. 5G mmWave (stand alone)	28/37/ 39 GHz (licensed)	Very high data rate; 5G Sub-6 GHz bands unavailable; Beamforming required for interference reduction and security; More friendly with LoS environments.	Limited, weak[1]	Limited[2], low[3]	PoC stage with demos in [41], [42], [47] High complexity and high cost for mmWave components [48], [49]	MmWave circuits and systems implementation and test challenges [50]- [53]; Antenna and product co-design challenges [26] [55]; Human body blockage issue [56]- [58]; High cost;
3. WiFi 2.4 GHz WiFi 5 GHz	2412-2484 MHz 5150-5835 MHz	Mainly for indoor applications [3]; Medium data rate for 802.11a/b/g/n/ac; High data rate for 802.11ac (WAVE 2), 802.11ax;	Indoor/ Outdoor, Strong (<5 GHz) and Medium (>5 GHz)	Long/ medium, low	802.11ac (WAVE 2) MU-MIMO routers available, medium cost; 802.11ax silicon announced [59]; 802.11ax router and AP announced [60], high cost;	Co-design challenge and resource competition with cellular systems; High complexity and power consumption, large antennas dimension due to high MIMO layers, e.g. 8×8 MIMO;
4. WiFi 60 GHz (WiGig)	57-71 GHz[4]	Point-to-point indoor communications; Very fast (802.11ad); Extremely fast (802.11ay);	Indoor, weak	Limited, <10 m[4]	802.11ad routers available, high cost [61]; 802.11ay silicon PoC announced [62], high cost;	Co-design challenge and resource competition with 5G cellular mmWave; Similar technical bottlenecks as tech. type 2;
5. 5G Sub-6 GHz CA	Wide and distributed, from 450 MHz to 6 GHz	Very high data rate; Spectrum segments at Sub-6-GHz bands available;	Wide, strong	Long, Medium	Similar to tech. type 1; More hardware resources to enable CA, very high cost;	Similar technical challenges as tech. type 1, with higher design complexity and hardware resources;
6. 5G mmWave CA	28/37/ 39 GHz (licensed)	Similar to tech. type 2; Multiple spectrum segments available at 5G mmWave bands;	Limited, weak[1]	Limited[2], Low[3]	Similar to tech. type 2; More hardware resources to enable CA, very high cost;	Similar technical challenges as tech. type 2, with higher design complexity and hardware resources;
7. 5G Sub-6 GHz & mmWave CA	450 MHz to 6 GHz, 28/37/ 39 GHz	Very high data rate; Shared spectrum at Band 46 available;	Limited, weak	Limited[2], low[3]	Based on readiness and maturity of tech. type 5 and 6; More hardware resources and high complexity, very high cost.	Based on similar challenges of tech. type 5 and 6, but with even higher design complexity and hardware resources;
8. 5G Sub-6 GHz LAA	450 MHz to 6 GHz, 5150-5835 MHz (unlicensed)	Very high data rate; Shared spectrum at Band 46 available;	Wide, strong/ medium	Long, medium	Similar to tech. type 5; More hardware resources and more complicate design to enable LAA, very high cost;	Based on similar technical challenges as tech. type 3 & 5, with higher co-design (Cellular&WiFi) complexity and more hardware resources such as antennas and chipsets;
9. 5G mmWave LAA	28/37/ 39 GHz, 57-71 GHz (unlicensed)	Similar to tech. type 2, with much higher data rate; Shared spectrum at mmWave available;	Limited, weak	Limited[2], low[3]	More advanced than tech. type 6; More hardware resources and more complicate design to enable LAA, very high cost;	Based on similar technical challenges as tech. type 4 & 6, with higher co-design (Cellular&WiFi) complexity and more hardware resources such as antennas and chipsets;
10. 5G Super-CA	450 MHz to 6 GHz, 28/37/ 39 GHz, 5150-5835 MHz, 57-71 GHz (unlicensed)	Extremely high data rate; Massive data transmission; Multi-task; Highest requirement for networks and infrastructure;	Indoor, weak	Limited[2], low[3]	Most advanced tech. type, depending on readiness and maturity of tech. type 1-9; Most hardware resources and most complicate design, highest cost;	Based on similar technical challenges as tech. type 5-9, with highest co-design (Cellular& WiFi) complexity and most hardware resources such as antennas and chipsets;

[1] Can be mitigated by increasing the density of smallcells, femtocells;
[2] Line of sight (LoS) distance depends on the maximum allowable EIRP of BS, MS, angle of arrival (AoA), and angle of departure (AoD) as well;
[3] The mobility also depends on the mobility and handover management schemes [63], beam search and tracking algorithms;
[4] Normally, a couple of meters of effective communication, for IEEE 802.11ad WiGig [[64], [65]. It is likely to have transmission distance extended, but the state-of-the-art IEEE 802.11ay silicon design achieves various distance (<3 m) under different modulation schemes [62].

become critical limiting factors in the 5G PHY layer design. In this section, we present a novel cost effective and space saving architecture that enables multiplexing of 5G cellular and WiFi/WiGig standards, with re-used antenna phased arrays. The system block diagram is depicted in Fig. 9, which facilitates mode switching according to

specific application scenarios, including the implementation of Super-CA.

Moreover, a detailed and complete wireless architecture is depicted in Fig. 10, which includes function blocks of 5G sub-6 GHz [43] (compatible with 2G/3G/4G), 5G high-order MIMO (sub-6 GHz 5G NR), 5G mmWave, IEEE
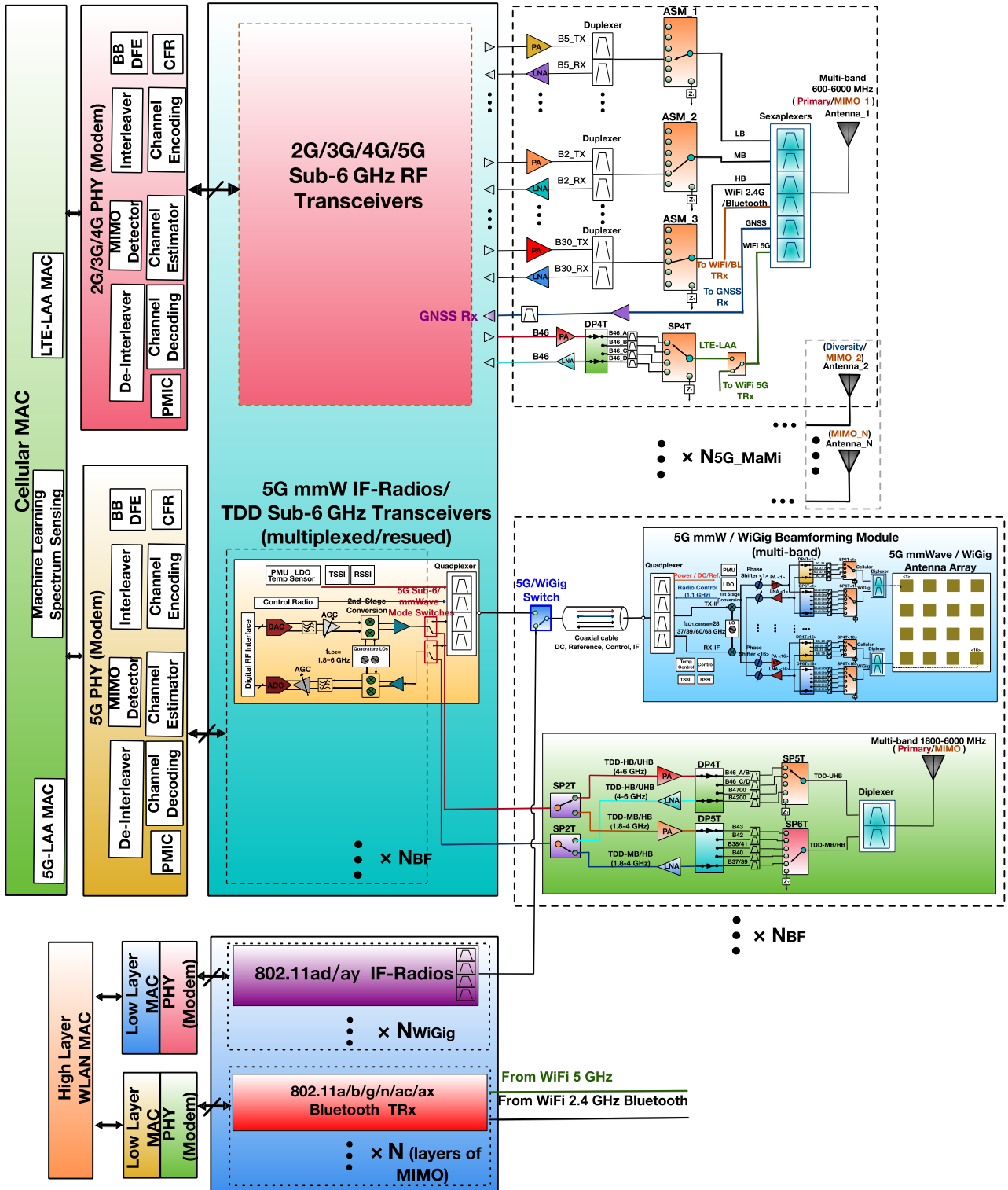
FIGURE 10. Multi-functional multi-standard 5G wireless system architecture.

802.11a/b/g/n/ac/ax, IEEE 802.11ad/ay WiGig, Bluetooth, GNSS, 5G-CA, 5G-LAA, etc. Next, the major function blocks for cellular, as well as cellular and WiFi/Wigig multiplexing are explained in details.

A. 5G SUB-6 GHZ COMMUNICATION

A multi-band antenna operating from 600 MHz to 6 GHz is used for a 5G sub-6 GHz front end and followed by a multiplexer. In the design case illustrated in Fig. 10, a sexaplexer

is proposed to enable a 6-way spectral division of sub-6 GHz to LTE low band (LB), LTE mid band (MB), LTE high band (HB), WiFi 2.4 GHz, global navigation satellite system (GNSS), and WiFi 5 GHz (3GPP Band 46). Each divided spectrum is routed to an individual antenna switch module (ASM) to realize further band selection. In Fig. 10, the drawings of RF chains for other cellular bands are skipped for simplicity. Such a topology can enable a 5G sub-6 GHz CA case through accommodating multiple sets of front-end components.

Moreover, a ''LTE-LAA/WiFi Switch'' is used to realize the mode switching between TDD Band 46 and WiFi 5 GHz. When the LTE-LAA (or 5G sub-6 GHz) working mode is initialized, the RF route between port 6 of the sexaplexer and a single-pole-four-throw (SP4T) is built. As shown in Fig. 10, a double-pole-four-throw (DP4T) is used to realize TDD downlink and uplink multiplexing, as TDD Band 46 is sufficiently wide that dividing it into 4 sub-bands with around 200 MHz each is more feasible and practical. As a result, 5G sub-6 GHz LAA can be formed by combing both the LTE LB/MB/HB and the shared unlicensed TDD Band 46.

However, implementing more CA combinations, or enabling multiple CA simultaneously working, necessitates more hardware resources such as RF front ends and RF transceivers. Regarding RF transceivers, more bands and higher layers of MIMO support indicate that more advanced architecture and design techniques need to be created. As shown in Fig. 10, Antenna_1, named as the primary antenna which is normally accommodated in the specific part of the UE rear housing such as the top part of UE, because it is usually not blocked by human hands. N_{5G_MaMi} (usually>8) sets of MIMO antennas, front ends, and RF transceivers are used to enable higher order 5G sub-6 GHz MIMO at the UE end. The performance and complexity of the MIMO detector, channel estimator, and channel coders/decoders of the 5G sub-6 GHz system are much higher than that of its 4G counterpart.

B. 5G MMWAVE COMMUNICATION

The implementation of 5G mmWave communication functions is based on the DPA-MIMO architecture [26]. The phased array antennas and mmWave beamformer are co-designed in one single beamforming module (BFM) that also performs the first-stage frequency conversion. The 5G-mmWave IF-Radios further process the signals of frequencies lower than medium bands (<6 GHz). Thin coaxial cables are used to connect the 5G mmWave BFMs and the 5G IF-Radios. For example, I-PEX cable is a miniature RF connecting cable with a diameter of 0.8 mm or less for high-frequency signals up to 6 GHz and widely used in contemporary wireless products such as smartphone, laptop, wireless router, etc. The coaxial cables carry a reference signal, a control signal, an IF signal, and deliver direct current (DC) power from 5G IF-Radios on the main logic board (MLB) to BFMs. These four types of signals are combined or split through quadplexers; besides, a well-defined frequency plan needs to
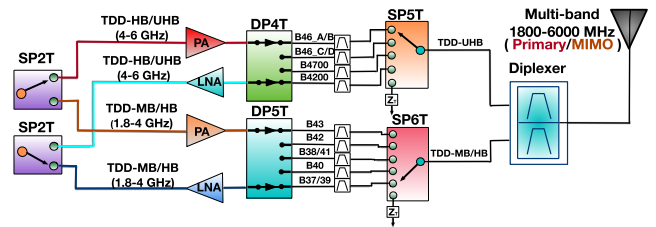
FIGURE 11. 5G TDD sub-6 GHz front-end and antenna module dedicated to 5G multiplexing/reuse.

be designed to improve the system signal integrity [26]. Other benefits of applying DPA-MIMO to the 5G UE design have been well motivated and presented in [26].

Furthermore, the entire 5G mmWave system consists of N_{BF} multiple BFMs and IF-Radios. The N_{BF} BFMs are arranged in the 5G UE rear housing following distributed approaches specified in DPA-MIMO design principles. A typical 5G UE mmWave design example [26] is redrawn in Fig. 13. There are two switches connecting the Quadplexer in the 5G mmWave IF-Radio which enable mode switching between 5G mmWave and 5G TDD sub-6 GHz. This enables flexible self-adaptive reconfiguration which copes with various application scenarios.

C. 5G MMWAVE IF-RADIO MULTIPLEXING AND REUSE

When 5G mmWave communication is not available or needed, the route between 5G mmWave IF-Radio and 5G mmWave beamforming module is closed by deselecting the quadplexer using ''5G sub-6/mmWave mode switches''. Correspondingly, the downlink/uplink paths between the 5G mmWave IF-Radio and the single-pole-double-throw (SP2T) of the 5G sub-6 GHz front-end modules is established. In this situation, the 5G mmWave IF-Radio is transformed to a new role of ''5G TDD sub-6 GHz transceiver'', to co-work with the 5G TDD-sub-6 GHz front-end modules.

It is predicted that 5G sub-6 GHz bands will play a crucial role in future 5G services, since many more TDD bands over 3 to 6 GHz will be commercially launched. In particular, considering the wide shared spectrum provided by TDD Band 46, it is therefore necessary to accommodate more hardware resources at TDD MB (1.8-2.7 GHz), TDD HB (2.7- 4 GHz), and TDD ultra-high band (UHB) (4-6 GHz), to enable higher layer of MIMO.

As shown in Fig. 11, a multi-band (1800-6000 MHz) antenna is followed by a diplexer that is connected with a single-pole-5-throw (SP5T) and a single-pole-6-throw (SP6T). The SP5T and SP6T realize the band selection for a majority of emerging 3GPP bands such as Band 37-43, Band 46 (divided into 4 sub-bands, namely B46_A, B, C, D), plus TDD bands yet to be released, such as B4200 (4000-4400 MHz) and B4700 (4500-4900 MHz).

Furthermore, TDD-HB/UHB PA and LNA (working at 4-6 GHz) are multiplexed through a double-pole-4-throw (DP4T) to TDD-HB/UHD band filters, while TDD-MB/HB
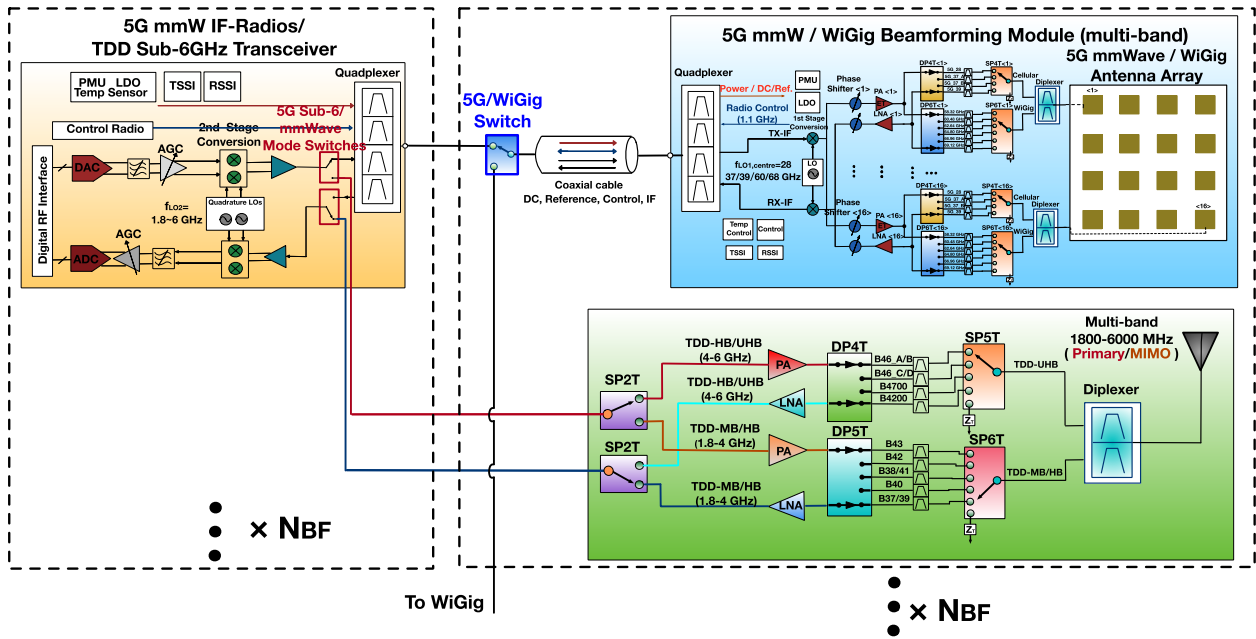
FIGURE 12. Enabling 5G mmWave uplink and 5G TDD Sub-6 GHz downlink simultaneously.

band filters are connected with TDD-MB/HB PA and LNA (working at 1.8-4 GHz) through a double-pole-5-throw (DP5T). By utilizing two groups of PA/LNA optimized at individual frequency bands, the design challenges of ultra-wide band otherwise using one PA/LNA can be alleviated. As a result, overall performance is improved. Eventually, two SP2T modules facilitate a flexible operation combination of 5G TDD sub-6 GHz bands.

From a higher system-level perspective, there are several benefits of reusing and multiplexing 5G mmWave IF radios. First, it enriches 5G CA and 5G LAA use cases by enabling higher-order sub-6 GHz MIMO. Second, a highly flexible and re-configurable hardware architecture can effectively reduce the hardware expense, and increase the cost-effectiveness. This can alleviate the hardware resource competence with other bands or standards.

In total, there are N_{BF} sets of 5G mmWave IF-Radios (5G TDD sub-6 GHz transceivers), 5G mmWave BFMs, and 5G TDD-Sub-6 GHz front-end modules. In one potential application scenario, there could be the situation that N out of N_{BF} sets of 5G mmWave IF-Radios (5G TDD sub-6 GHz Transceivers) work with N sets of 5G TDD-Sub-6 GHz front-end modules to realize 5G TDD Sub-6 GHz communication, while the remaining $(N_{BF}-N)$ sets of 5G mmWave IF-Radios collaborate with $(N_{BF}-N)$ sets of 5G mmWave BFMs to operate 5G mmWave communications.

On the other hand, the two mode switches, i.e., the uplink switch and the downlink switch, do not have to enable the same mode (either mmWave mode or TDD sub-6 GHz) at the same time. When downlink works in 5G mmWave mode, uplink can still work in 5G TDD-Sub-6 GHz mode and vice versa. This can further improve the flexibility of 5G UE

operation, thus being able to adapt to more diverse application scenarios. An example is illustrated in Fig. 12, where the uplink mode switch creates a 5G mmWave path, while the downlink mode switch enables the TDD Band B4200 to be tuned and received.

D. CELLULAR AND WIFI/WIGIG MULTIPLEXING AND REUSE

Cellular and WiFi compete for limited hardware resources at the UE end (e.g., at 2.4/5 GHz band). This competition is more severe when IEEE 802.11ax is deployed with higher modulation and MIMO order. Another challenge comes with implementation of IEEE 802.11ad/ay WiGig.

1) As presented in [26] and re-illustrated in Fig. 13, eight identical 5G mmWave BFMs for cellular communications would be already tightly packed in the rear housing of a 5G UE (smartphone). Such a distributed placement can assure an excellent and robust spherical coverage cumulative distribution function (CDF) [66], [67]. However, it may be impractical to squeeze in WiGig modules unless several cellular BFMs are replaced with WiGig ones. Compromising cellular performance is the last option if better coexisting approach can overcome this issue.

2) In the proposed architecture, we demonstrate a highly flexible and re-configurable circuits and systems architecture which enables the reuse and multiplexing of beamforming functions for both cellular and WiGig technologies. As illustrated in Fig. 9, a "5G Cellular/WiGig Switch" is inserted between coax cables and cellular IF-radios, as well as WiGig IF-radios. As a result, the mmWave beamforming module can
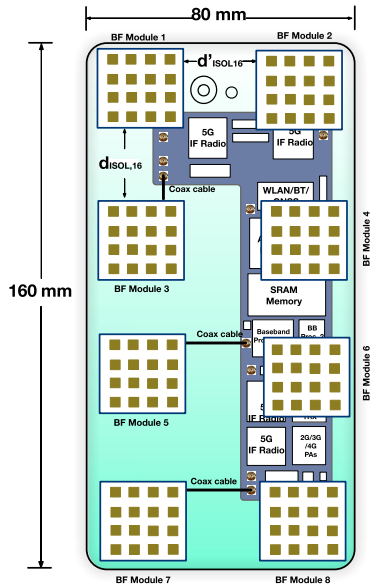
FIGURE 13. 5G mmWave cellular hardware design example [26].

be multiplexed for both WiFi/WiGig and 5G cellular functionality.

3) Furthermore, cellular IF-radios can be also reused for cellular sub-6 GHz front ends and antennas through

enabling the switches connected to them. Consequently, 5G mmWave cellular, WiGig, and 5G sub-6 GHz cellular can be reconfigured. In particular, WiGig and sub-6 GHz cellular functions could be simultaneously activated on request.

4) One of the prerequisites to enable the aforementioned feature is the BFMs's capability to operate at a very wide range of frequencies above 6 GHz, which is ideally from 28 to 71 GHz. The second prerequisite is that the WiGig function should also be implemented using Split-IF architecture.

5) About the possible WiGig implementation, as illustrated by a more detailed design example in Fig. 14, it is based on the DPA-MIMO architecture via reusing the BFMs through a multiplexing approach. The total number of WiGig IF-Radios, N_{WiGig}, is flexible, but can not be bigger than N_{BF}. Additionally, it is decided by various factors such as, marketing schemes, peak data rate required, hardware space and resources. Similar to 5G mmWave IF-Radios, WiGig IF-Radios are also implemented on the 5G UE's MLB. Furthermore, with respect to WiFi 2.4/5 GHz technologies, both high modulation (1024-QAM) and high MIMO layer need to be supported. Therefore, N_{WiFi_MIMO} can be as high as 8.
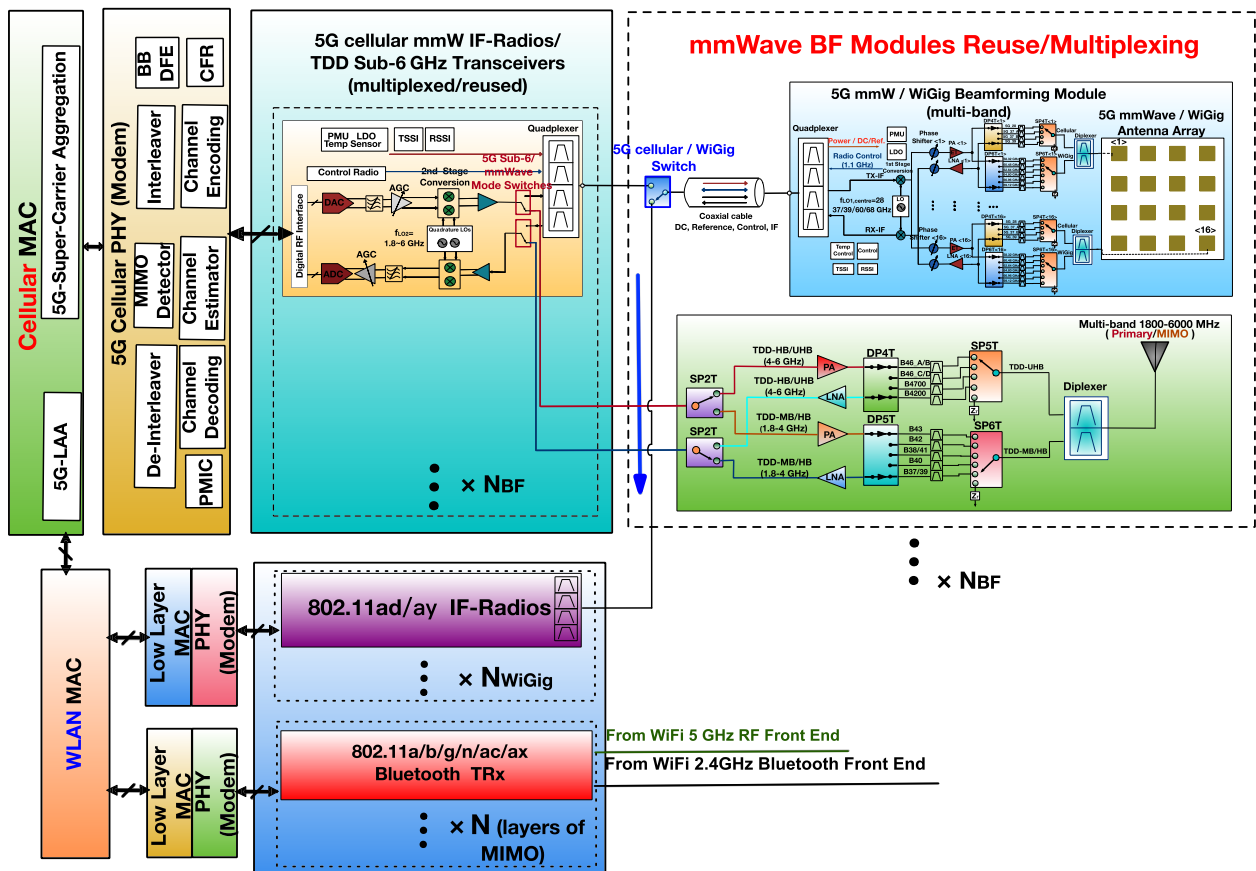

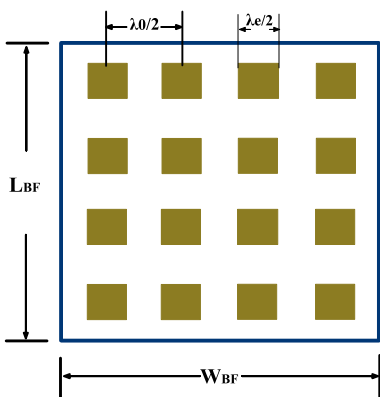**FIGURE 14.** 5G UE WiGig solution based on multiplexed DPA-MIMO architecture.

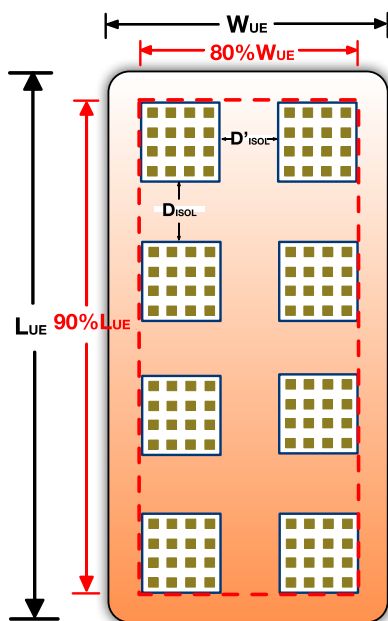**FIGURE 15.** Top view of phased array design example with patch antenna elements.

FIGURE 16. Top view of phased array design example with patch antenna elements.

E. UE AND BFM DIMENSIONS AND IMPLICATIONS

A critical system-level constraint of 5G UE design is hardware space. It is predicted that, in the near future, more and more trendy wireless technologies are required to be integrated on one single UE. On the other hand, aesthetic appearance for 5G hand-held devices cannot be compromised due to user experience and marketing reasons. Take a mainstream 5.5-inch smartphone for instance, the popular dimensions are around 160mm × 80mm × 8mm.

Assuming that the BFM whose top view is depicted in Fig. 15, the phased array contains A_{ANT} rows, B_{ANT} columns of antenna elements. Therefore the total antenna elements, $N_{ANT} = A_{ANT} \times B_{ANT}$. A 5G UE design example is illustrated in Fig. 16 where A_{ANT} is 16. The width and length of BFM can be estimated by

$$L_{BF} = A_{ANT} \times \lambda_0/2 \qquad (1)$$

$$W_{BF} = B_{ANT} \times \lambda_0/2, \qquad (2)$$

where λ_0 is the free-space wavelength.

Furthermore, in one single UE device, presumably there are A_{BF} rows and B_{BF} columns of BFMs. Therefore the total number of BFMs, N_{BF}, is equal to $A_{BF} \times B_{BF}$. In terms of the DPA-MIMO design principles [26], in order to assure a good spatial multiplexing gain plus thermal dissipation, the isolation spacing (edge-to-edge distance of beamforming modules), D_{ISO}, should be at least 1.5 times λ_0.

As illustrated in Fig. 16, L_{UE} and W_{UE} stand for the length and width of the UE. Furthermore, about 90% of L_{UE} and 80% of W_{UE} are assigned to the footprint of the BFMs, which means that 72% of the effective area of the rear housing is occupied by BFMs. On the other hand, the remaining 28% of the area is used to accommodate sub-6 GHz antennas, sensors, cameras, etc.

The constraint equations of BFMs arrangement and the UE dimension can be derived as follows:

$$A_{BF} \times L_{BF} + (A_{BF} - 1) \times D_{ISO} \leq L_{UE} \times 90\%, \qquad (3)$$

$$B_{BF} \times L_{BF} + (B_{BF} - 1) \times D_{ISO} \leq W_{UE} \times 80\%, \qquad (4)$$

where L_{BF} and W_{BF} can be calculated using (1), and (2), and D_{ISO} is set to $1.5\lambda_0$. Hence, (3) and (4) are written as

$$A_{BF} \times A_{ANT} \times \lambda_0/2 + (A_{BF} - 1) \times 1.5 \times \lambda_0 \leq L_{UE} \times 90\%, \qquad (5)$$

$$A_{BF} \times A_{ANT} \times \lambda_0/2 + (A_{BF} - 1) \times 1.5 \times \lambda_0 \leq L_{UE} \times 90\%. \qquad (6)$$

When the carrier frequency and N_{ANT} are fixed, the maximum number of BFMs that can be accommodated in a UE is determined. Consequently, the maximum supported spatial streams can be obtained; this is directly related to the UE dimension and carrier frequency.

Furthermore, the relation between free space path loss (FSPL) and wavelength, and the relation between beamforming gain and antenna elements quantity per BFM are well defined. The Friis transmission equation with ideal beamforming gain induced is given by

$$P_r = P_t + 10\log(N_{ANT}) + 10\log(\frac{\lambda_0}{4\pi d})^2 \qquad (7)$$

where P_t is the output power when omni-directional antenna is used, and d stands for the distance. As $N_{ANT} = A_{ANT} \times B_{ANT}$, (7) can be further transformed to

$$P_r = P_t + 10\log(A_{ANT} \times B_{ANT}) + 10\log(\frac{\lambda_0}{4\pi d})^2 \qquad (8)$$

which, by inducing (1) and (2), can be further formulated as

$$P_r = P_t + 10\log(\frac{4L_{BF} \times W_{BF}}{\lambda_0^2}) + 10\log(\frac{\lambda_0}{4\pi d})^2$$

$$= P_t + 10\log\frac{L_{BF} \times W_{BF}}{4\pi^2 d^2}. \qquad (9)$$

As observed in (9), the signal strength (transmit and receive) has no correlation with carrier frequency, but only depends on the dimension of BFM (phased array) and communication distance. Furthermore, the spatial multiplexing gain can also
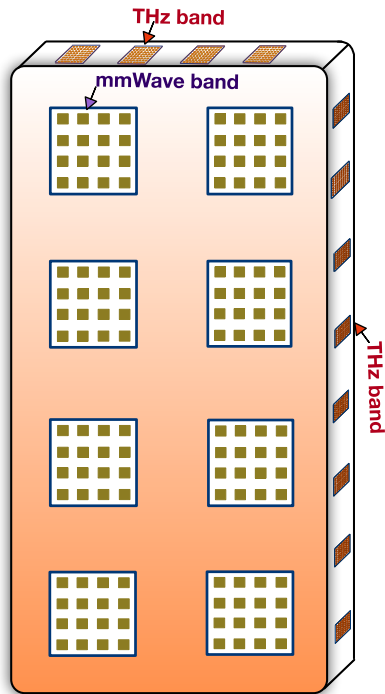
FIGURE 17. A conceptual UE antenna system design accommodating both mmWave and THz beamforming modules.

be determined as long as the dimension of BFM and UE are defined. Take the mmWave DPA-MIMO architecture for example, the beamforming gain, SMG, SE, and other wireless performance are well defined if the 5G UE dimension is given. Although more hardware area is desired to mitigate the challenges of 5G mmWave UE design, UE dimension and weight have direct impact on user experience and UE cost, which needs careful market research.

In addition, the antenna and beamforming modules may be accommodated not only in the UE's rear back housing, but also in the side narrow frame of a hand-held device [68], which can enhance the spherical coverage and mitigate the human body (hand) blockage issue. On the other hand, considering the typical thickness (e.g., 6-10 mm) of contemporary hand-held devices, it would be challenging to place mmWave beamforming modules but feasible to integrate beamforming modules working at the THz band (0.1 THz to 10 THz). For example, an 8×8 phased array operating at 338 GHz requires an implementation area smaller than 5×5 mm according to the design and fabrication in [69]. As further illustrated in Fig. 17, there are 4 and 8 THz-BFMs on the short side frame and long frame, respectively.

V. BEAMFORMING, ANTENNA AND INTEGRATED CIRCUITS

In this section, more in-depth investigation and analysis of critical hardware architectures, circuits and systems that facilitate cellular and WiFi co-enabling functions at 5G high bands are conducted.

A. Beamforming Architecture

According to the categorization of beamforming techniques summarized in [70], there are mainly four beamforming array architectures, namely, RF-path beamforming, LO-path beamforming, baseband (BB) beamforming, and digital beamforming. The phase shifter design of each type is quite different, and their advantages and disadvantages for RF system design and implementation are summarized in Table 3.

From a hardware design standpoint, RF beamforming is more suitable for high GHz applications, with lowest complexity in LO, mixer, and baseband modem calibration for wideband beamforming whereas its SNR performance is degraded due to the loss caused by attenuation at high GHz frequencies. The other three beamforming schemes lead to more complicated designs of LO, mixer and calibration algorithms.

On the other hand, hybrid beamforming technique has become a promising approach of reducing the hardware cost and training overhead in massive MIMO systems as it can take advantage of both lower-dimensional digital processing and large-dimensional analog pre/post-processing [73], [74]. Compared to fully digital beamforming (DBF) [71] which can achieve higher magnitude and phase resolution, and hence higher capacity, hybrid beamforming permits a flexible trade-off between the hardware resources and wireless performance [75], [76].

Furthermore, hybrid beamforming entails either fully-connected structure or partially-connected structure as illustrated in Fig. 18. The hardware cost and power consumption of the partially-connected hybrid beamformer are significantly lowered since power combiners/splitters can be skipped and the total number of RF phase shifters is reduced by N_{BF}^t times, although some degradation in spectral efficiency (SE) is observed. Therefore, the partially-connected structure is more realistic and valuable for the user equipment design. In fact, the DPA-MIMO architecture is a specific manifestation of the partially-connected structure as each RF chain is dedicated to one specific sub-array.

B. MMWAVE ANTENNA ARRAY

Based on the DPA-MIMO architecture, one technical hurdle of enabling wideband operation lies in the multi-band, broadband antenna array design, particularly when supporting multiple bands, e.g., 28 GHz, 37 GHz, 39 GHz, 60 GHz, and 71 GHz, is required.

In [77], authors have presented a 4×4 broadside radiation array and a 4×4 beam-scanning array, which exhibit a flat gain response of around 19 dBi from 23 to 32 GHz, with good out-of-band rejection performance. The FBW is as large as 32.7%, and this topology can be extended or enhanced for 28/38 GHz bands applications, but further efforts are needed for bands above 60 GHz. Moreover, a dual-band dual-polarized (DBDP) array is reported in [78] and redrawn in Fig. 19. It achieves two operation bands from 5.05 to 5.3 GHz and from 9.6 to 10.3 GHz, respectively,

TABLE 3. Comparison of the four beamforming architectures for an N × N array system [70].

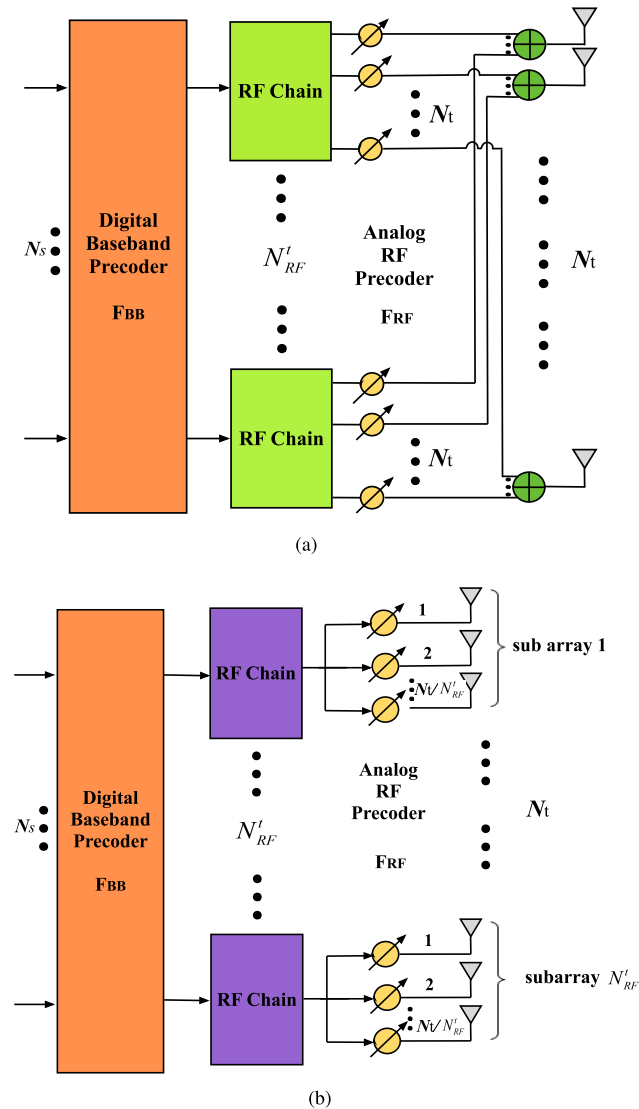| Architecture References	Low GHz	High GHz	Wideband Beamforming	Receiver SNR	LO Complexity	Mixer Complexity	Phase Shifter Resolution	Number of ADC	Number of DAC	Modem Calibration Complexity
RF	-	+	+	-	+	2	+/-	2	2	+
LO	+	+/-	-	+	-	2N	-	2	2	-
Baseband	+	+	-	+	-	2N	+	2	2	-
Digital	+	-	-	+	-	2N	+	2N	2N	-

(a)

(b)

FIGURE 18. Block diagram of (a) full-complexity hybrid beamforming, and (b) reduced-complexity hybrid beamforming.

with a demonstrated radiation efficiency higher than 80%. This topology might be a potential structure for multi-band and narrow-band based mmWave antenna arrays. Furthermore, in [79], a dual-band and co-aperture antenna array implemented in substrate integrated waveguide (SIW) and stripline (SLIN) technologies is presented. It has used a mainstream four-metal-layer, low-cost printed circuit board (PCB) to design and fabricate a phased array providing E-band
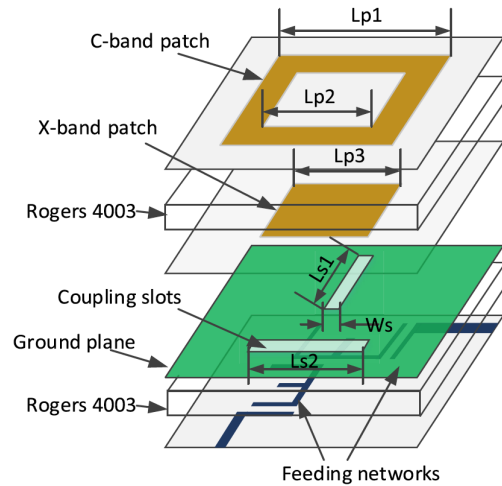

FIGURE 19. Explode view of dual-band dual-polarized (DBDP) antenna element [78].

(71-86 GHz) and local multipoint distribute service (LMDS) band (25-32 GHz). The core idea is to stack two types of antenna elements vertically, and particularly, the LDMS band antenna element should have enough space to accommodate the E-band element in order to give spacious opening.

Both [78] and [79] have leveraged a multi-layer structure to stack up two types of antenna elements targeting at two frequency bands. With respect to the topology in [79], unlike [78], the element spacing varies, according to high and low bands. Therefore, the element spacing of LDMS band is around two times as E-band, which may help facilitate a wider bandwidth at both bands. On the other hand, [78] has specified a fixed element spacing which is equal to 0.42 and 0.8 wavelength at 5.2 and 10 GHz, respectively.

From the investigation above, the BF module design needs to satisfy several aspects. First, given that an antenna array structure similar to the one in [79] is used, a multi-band, broadband antenna array with fixed element spacing can satisfy the technical specifications. As illustrated in Fig. 20, a diplexer is used to connect one antenna element of the broadband phased array with an RF switch. Low mmWave bands (28-40 GHz) for 5G cellular and high mmWave bands (57-71 GHz) for WiGig are separated. Through a SP4T and band filters, four 5G bands, namely 5G_28, 5G_37A, 5G_37B, 5G_39, are selected correspondingly. Furthermore, a SP6T enables the band selection of 6 WiGig bands with center frequencies at 58.32 GHz, 60.48 GHz, 64.80 GHz,
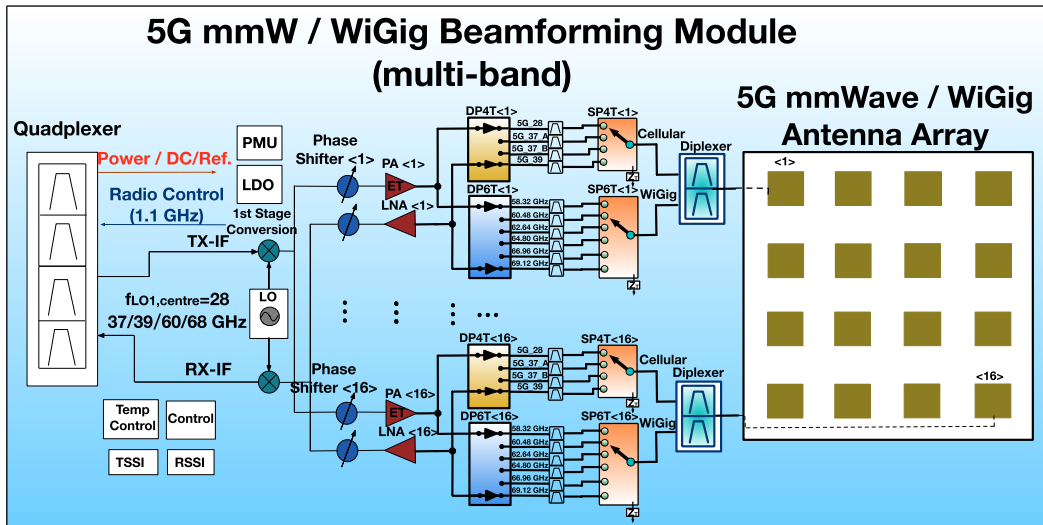
FIGURE 20. 5G mmWave BF module design with a single multi-band antenna array.
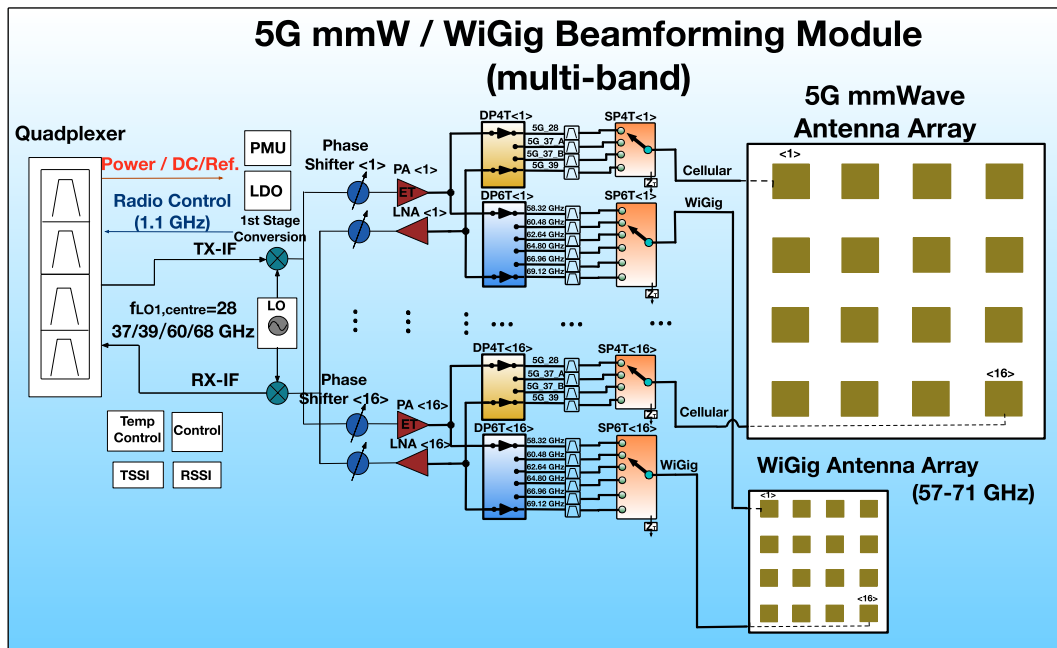

FIGURE 21. 5G mmWave BF module design with separate antenna arrays.

66.96 GHz, and 69.12 GHz. A DP4T and DP6T are used for TDD operation and mode switching of 5G mmWave and WiGig, and only one wideband PA and one wideband LNA are required. Moreover, a multi-band frequency synthesizer operating at a wide frequency range is used to realize the frequency conversion of the listed mmWave bands, 28/37/39/60/68 GHz, to the targeted IF-Radio frequency. Therefore, only one band is exclusively operating, for either uplink or downlink.

On the other hand, if a multi-band broadband antenna array is temporarily unavailable, an alternative structure is given as in Fig. 21. As observed, the 5G cellular antenna array and WiGig antenna array are separated, which might facilitate higher performance of the beamforming. Moreover, a diplexer is skipped for each antenna element, and thus the cost and insertion loss are reduced. However, such a BFM has a bigger area and causes an impact on the UE product and appearance design.

Moreover, it is meaningful to emphasize that a square-shaped 4×4 antenna array is used instead of 2×8 array or any other ones based on rectangular shape. This is mainly because, unlike a laptop, a 5G handset UE can be placed
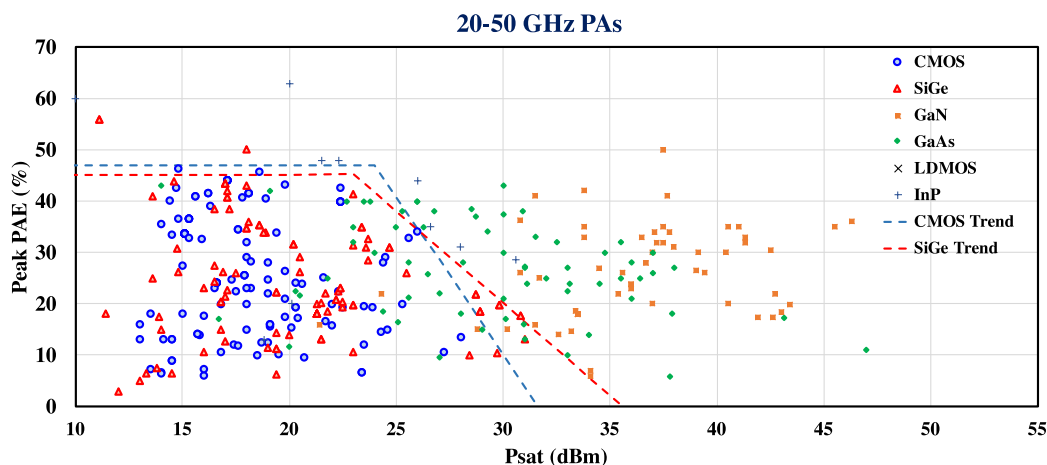
FIGURE 22. Perfromance of power amplifiers at frequency range of 20 to 50 GHz, published since 2000.

vertically and horizontally or rotated more frequently and randomly by the user. Additionally, on-chip antennas have been investigated and verified in recent years [80], particularly for mmWave high bands and THz applications. However, for mmWave applications at a lower frequency range (<100 GHz), the cost-efficiency of on-chip antenna solutions is still outperformed by other solutions such as low temperature co-fired ceramics (LTCC) [81], multi-layer organics (MLO) [82], liquid crystal polymer (LCP) [83] or SIW solution [84] due to relatively low radiation efficiency [85]–[88], low yield, issues related to manufacturing and testing, high cost, etc.

In order to effectively enable the wideband beamforming for multiple bands on 5G UE devices, the performance of critical integrated mmWave/sub-mmWave components, such as power amplifier, low noise amplifier, local oscillator (LO), and phase shifter, should be carefully investigated and specified.

C. POWER AMPLIFIER
As the power amplifiers of both sub-6 GHz and hyper-6 GHz are required on a 5G UE device, the 5G PA system design becomes more complicated and challenging to cope with the energy efficiency and overall PA system's reliability such as thermal performance. Based on the status-quo and future trend of research and development, complementary-metal-oxide-semiconductor (CMOS), silicon germanium (SiGe), gallium nitride (GaN), germanium arsenide (GaAs), laterally diffused metal oxide semiconductor (LDMOS), and Indium Phosphide (InP) are competitive candidate IC processes for integrated PAs operating at 5G high bands.

Nonlinear distortion in amplitude and phase of a PA are mainly dominated by AM-to-AM distortion and AM-to-PM distortion, respectively. Nonlinear distortion out of the band can result in significant leakage to adjacent channel, and therefore degrades the adjacent channel leakage ratio (ACLR) performance, while nonlinear distortion in-band can lead

to deterioration of error vector magnitude (EVM). Usually, operating at higher frequencies makes nonlinear distortion more pronounced.

Based on a power amplifier performance survey [89], the performance of integrated PAs working at 20-50 GHz, published from 2000 to present, is summarized and given in Fig. 22. As illustrated, at the frequency of interest, PAs designed using CMOS and SiGe processes demonstrate satisfactory peak power added efficiency (PAE) (higher than 30%) when the saturated output power, P_{sat}, is lower than 25 dBm, while PAs designed by GaN and GaAs processes demonstrate much higher performance. On the other hand, the maximum effective isotropic radiated power (EIRP) is regulated to be 43 dBm for mobile stations (MSs) by the FCC [90], as calculated, in a beamforming module where a 16-element phased array is employed, the maximum output power of each PA is limited to 19 dBm [26].

Several CMOS/SiGe PAs examples are summarized here. A 5G mmWave multi-band Doherty PA prototype was presented with outstanding PAE and power back-off efficiency [51]. A 5G K/Ka-Band PA prototype with high peak PAE (41.5%) at very wide frequency range (18-29 GHz) was also presented in [91]. Furthermore, [92] presents a 46 GHz PA with 42.5% peak PAE and 22.4 dBm P_{sat}. Reference [93] demonstrates a continuous-mode hybrid class-F/F-1 power amplifier operating at a very wide frequency range from 23.5 to 41 GHz, with 46% peak PAE. In addition, at WiGig bands, a CMOS PA demonstrates a 28.3% peak PAE with a P_{sat} of 19.4 dBm [94].

On the other hand, high peak to average power ratio (PAPR) of the popular modulation schemes adopted today, such as OFDM, makes power back-off significantly high. Some crest factor reduction (CFR) strategies including but not limited to, digital predistortion (DPD) [95], RF predistortion (RFPD) [96], doherty PA [51], [97], envelop tracking, can be judiciously applied to different design cases and application scenarios.

Based on the above investigation, current PAs designed in CMOS and SiGe at 5G high band frequencies, can theoretically meet the performance requirements. These two processes are more appealing than other processes due to lower cost and higher integration level, particularly for 5G UE design.

D. LOW-NOISE AMPLIFIER

Wideband LNAs for 5G high bands are important as they largely determine the oveall noise factor (F_{tot}) and linearity of the entire receiver path and thus signal-to-noise ratio (SNR) and bit error rate (BER). The noise factor is given by

$$F_{tot} = 1 + (F_1 - 1) + \frac{F_2 - 1}{A_{P1}} + \frac{F_3 - 1}{A_{P1} A_{P2}} + \ldots + \frac{F_m - 1}{A_{P1} \ldots A_{P(m-1)}}, \tag{10}$$

where $A_{P(m-1)}$ denotes the available power gain of the previous stage ($(m-1)^{th}$ stage). Since LNA is located at the second stage after the ASM module but before the phase shifter that normally introduces the attenuation (loss), a higher LNA gain is desired to suppress the overall noise factor of the RX path, and increase the dynamic range. On the other hand, the LNA linearity can be indicated by an important metric known as the third order input intercept point (IIP3), and the total IIP3 has the following expression:

$$\frac{1}{A_{IIP3,tot}^2} \leq \frac{1}{A_{IIP3,1}^2} + \frac{G_1^2}{A_{IIP3,2}^2} + \frac{G_1^2 G_2^2}{A_{IIP3,3}^2} + \ldots + \frac{G_1^2 G_2^2 \ldots G_{m-1}^2}{A_{IIP3,m}^2}, \tag{11}$$

where G_{m-1} is the gain of the $(m-1)^{th}$ stage.

Furthermore, in a 5G system where RF bandwidth is significantly enlarged, gain flatness of the RX path and LNA is a serious concern and should be optimized in order to reduce the calibration complexity. As wireless standards become more diverse and the total number of frequency bands increases, integrating multiple LNAs and PAs altogether in the RF front end is difficult to avoid.

Authors of [98] proposed a very wide band (66.7% fractional bandwidth (FBW)) mmWave LNA based on 2-stage cascade topology, operating from 70 to 140 GHz, with a high gain and low noise figure. A 4-stage common source (with transformer-based Gm-boosting method) based 54.4 to 90 GHz LNA is demonstrated in [99] possessing 49.3% FBW and good FoM. However, as for the expected LNA in our proposed architecture, which covers a wide frequency range from 28 to 71 GHz (equivalent to 86.8% FBW), a more advanced and competent integrated LNA design is highly desired, while being still feasible, for current advanced III-IV compound processes. For example, an LNA designed in InP-HEMT process [103] back in 2010, can achieve a competitive FoM of 18.3 to 27.9, which is several times higher than the mmWave LNAs in [98]. Furthermore, in terms of the work presented in [100], a low-power 2-stage LNA achieves 8.5 dB gain 28 GHz, 6 GHz bandwidth, with a minimum noise figure of 2.7 dB. In addition, a 24–44 GHz ultra wideband (UWB) LNA is proposed with 65% 3dB bandwidth

and low noise figure (< 5.5 dB) over the frequency of interest [101]. As IC design techniques and processes advance, more low-cost high-performance wideband mmWave LNAs will be available to facilitate multi-band 5G UE products.

E. PHASE SHIFTER

Beam steering and siodelobe suppression are two critical performance indexes of a phased array, and the phase shifter design influences them. For example, 5-degree and 22.5-degree phase shift quantization/resolution can result in a sidelobe suppression of 18.5 dB and 15 dB, respectively [49]. On the other hand, minimizing the phase error can reduce the beam steering errors, beam shape distortion and calibration complexity. Beam switching speed that mainly depends on the switching speed of the phase shifter largely affects the beam training and searching capability particularly in a highly mobile environment. For example in [49], a 4-ns beam switching speed is recorded.

The performance loss due to the phase-shifting error and gain error, has been numerically analyzed in [102]. With a phase-shifting error of 5° and gain error of 1 dB, the sum rate has seen nearly 50% degradation when SNR is 25 dB.

For the RF phase shifter connected to either LNA or PA, if it has low insertion loss (or even some gain) and low variation in loss, an LNA and/or PA with very high gain is not necessary, but programmable gain settings are preferred. Furthermore, the RF phase shifter requires sufficient linearity, because the receiver path needs to cope with strong interferers which usually happen after the signal combining. Moreover, at the transmitter, phase shifters should not limit the linearity and output power.

According to [70], phase and amplitude control circuits can be mainly categorized into six types, namely, reflective-type phase shifter (RTPS), loaded-line phase shifter (LLPS), switched-delay phase shifter (SDPS), Cartesian vector modulator (CVM), LO-path phase shifter (LOPS), phase-oversampling vector modulator (POVM). The performance of phase shifters developed in recent years are summarized and compared in Table 4.

F. LOCAL OSCILLATOR SIGNAL GENERATION

With respect to the LO generation for 5G systems, unlike the 4G LO which is typically implemented on top of the sub-6 GHz phased-locked loop (PLL) with wideband voltage-controlled oscillators (VCOs) [114]–[116], the 5G LO generation should cover a wide range of frequencies including mmWave bands, e.g., 28 GHz/37 GHz/39 GHz/60 GHz/68 GHz/71 GHz, while maintaining good performance of phase noise and phase error.

In a TDD system, the phase noise produced by a TX LO can be easily spilled over into the receiver band of another UE device, and the phase noise specification and frequency offset can be derived from the maximum integrated noise that can be tolerated in channel and distance between TX and RX [117]. While for an FDD system, the TX signal leaks into the RX path of the same UE terminal, and the maximum noise

TABLE 4. Comparison of state of the art phase shifter designs.

Architecture and Reference	Frequency (GHz)	Process	Phase Resolution	Phase Coverage (deg.)	RMS Phase Error (deg.)	Power (mW)	Typical Gain (dB)	Area (mm^2)
RTPS [104], 2008	60	65 nm CMOS	4-bit	156	9.2	0	-9.4	0.2
RTPS [105], 2009	60	0.13μm SiGe BiCMOS	4-bit	180	5	0	-7.5	0.28
STPS [106], 2010	60	90 nm CMOS	2-bit	360	10	0	-7	0.032
STPS [109], 2013	60	65 nm CMOS	6-bit	360	2–10	0	-2	0.34
STPS [110], 2016	28	0.13μm SiGe	5-bit	190	0.6	0	-9.3	0.18
STPS [49], 2017	28	0.13μm SiGe	5.4-bit	210	1.5	0	–	0.67
STPS [100], 2018	24–30	45 nm CMOS	6-bit	360	5.6	0	-2.5	–
Dual-Vector [111], 2016	28–32	120 nm SiGe BiCMOS	4-bit	360	5.4	136.5[1]	9.4[1]	0.45[2]
Vector Modulator [107], 2017	87.4 (78.8–92.8)	65 nm CMOS	4-bit	360	9.4	21.6	2.3	0.12
Vector Summing [108], 2018	28	65 nm CMOS	9.4-bit[3]	360	0.54	25.2	-3.7	0.32
CVM [112], 2007	24.6	0.13μm CMOS	4-bit	360	13	11.7	-4.6 – -3	0.14
CVM [113], 2010	60	65 nm CMOS	4-bit	360	7	78[4]	12[4]	1.6[5]
CVM [53], 2018	25–30	65 nm CMOS	5-bit	360	4	27.5[6]	34[6]	0.32[7]

[1] Entire RX front end of one-element
[2] Estimated area per front-end element
[3] Calculated from phase error. 0.54 degree phase-error corresponds to a phase resolution of 9.4-bit. Estimated from paper. Results measured at only 28 GHz
[4] One RX path including LNA, phase shifter and combiner
[5] Including bonding pads and two RX paths each of which consists of a LNA, a phase shifter, and part of a combiner
[6] Single element of full receiver link
[7] Estimated equivalent chip area per antenna per stream

tolerated by the RX depends on the noise figure of the RX and the duplexer's isolation performance. It is worth mentioning that, since direct-conversion architectures are popularly applied to mmWave transceivers, generating precise I/Q components is particularly critical. Otherwise the I/Q phase and amplitude imbalances can degrade the image rejection ratio (IRR) and the error vector magnitude. The IRR is formulated as follows [123]:

$$|IRR| = \left| \frac{10^{\frac{\Delta A}{10}} + 2 \cdot 10^{\frac{\Delta A}{20}} \cos\Delta\theta + 1}{10^{\frac{\Delta A}{10}} - 2 \cdot 10^{\frac{\Delta A}{20}} \cos\Delta\theta + 1} \right|, \qquad (12)$$

where ΔA is the gain error in dB and $\Delta\theta$ is the phase error in radians between I and Q paths. Furthermore, the most important contributors to the degradation of EVM are namely, LO phase noise, LO leakage, gain flatness of receiver path and I/Q imbalances including LO path. According to [62], IRR is required to be better than 35 dBc so that a BER of 10^{-3} can be achieved on 64-QAM modulation. As calculated, such an IRR corresponds to less than 0.3-dB gain mismatch and less than 2-degree phase mismatch. Such an IRR performance needs to be maintained over 5G broad bandwidths and cope with the variances introduced by the process, voltage and temperature (PVT). A quadrature LO generator designed in 55-nm CMOS process demonstrated an IRR better than 40 dBc over the frequency from 28 to 44 GHz when measured under a wide temperature range from 5° to 120°.

When the carrier frequency moves up to mmWave, LO generation is more challenging and complicated. Fig. 23 illustrates the generic block diagram of a typical PLL frequency synthesizer that is normally used for LO generation in contemporary wireless devices. Such an LO generator
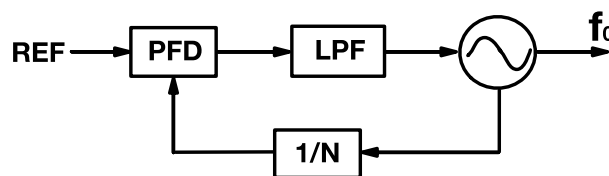

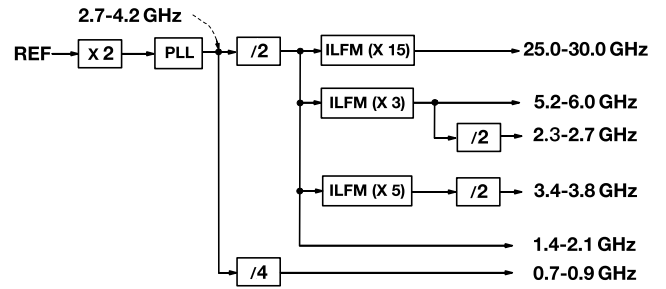**FIGURE 23.** Block diagram of a typical phase-locked loop frequency synthesizer for LO generation.

includes a reference (REF) signal (provided by crystal oscillator, XO), a phase/frequency detector, a loop filter (LPF), a divide-by-N frequency divider, and a VCO. When the carrier frequency runs at mmWave, the large PLL divider ratio, N, and large loop bandwidth will make the XO phase noise more critical.

Some mainstream mmWave LO generation strategies are illustrated here. As depicted in Fig. 24(a), a fractional-N mmWave PLL frequency synthesizer uses a delta-sigma modulator to reduce fractional spurs. However, several difficulties lie in the mmWave oscillators; for example, the parasitic capacitance takes a large portion of the small tank capacitance and the quality factor (Q-factor) of the tuning capacitor (also known as varactor) is low, which further limits both the turning range (TR) and lowers phase noise performance [118]. Moreover, the mmWave frequency divider is challenging to design considering a large TR required. In order to alleviate these challenges, a frequency multiplier is used in the topology illustrated in Fig. 24(b). However, designing a high frequency multiplier is another challenging task involving trade-offs between locking range and power consumption.

(a)

(b)

(c)

(d)
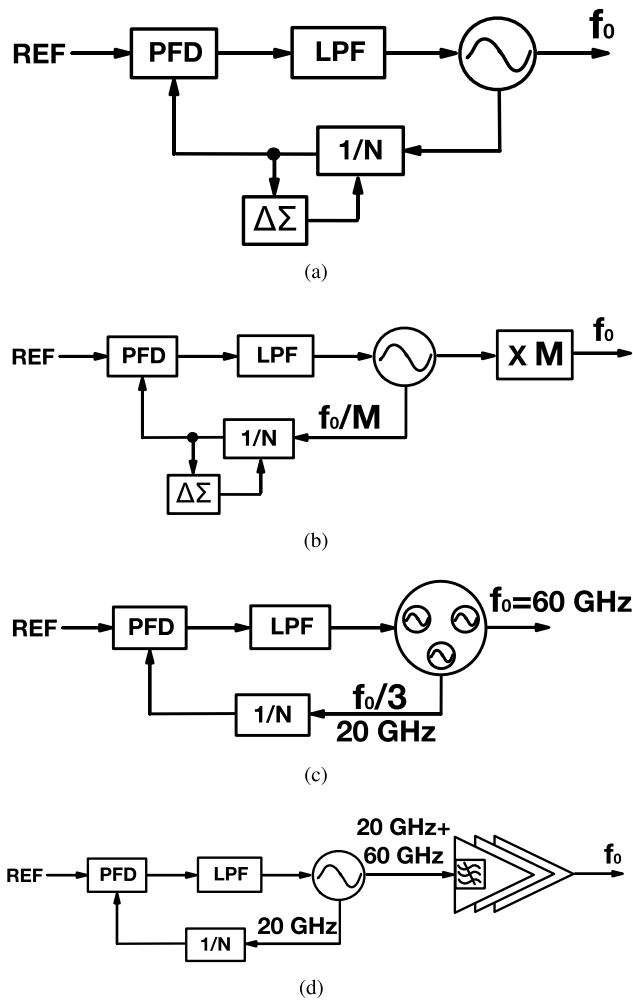
FIGURE 24. (a) fractional-N mmWave PLL frequency synthesizer, (b) mmWave PLL frequency sysnthesizer with multiplier, (c) triple-push VCOs based PLL frequency synthesizer [119], and (d) mmWave PLL with harmonic boosting and extraction [120].

FIGURE 25. Block diagram of 5G multi-band LO plan and LO generator [122].

Therefore, a frequency synthesizer topology based on the N-push VCOs is implemented to bypass the design of both high frequency multipliers and dividers. Fig. 24(c) illustrates a PLL that accommodates a triple-push VCO [119] that has coupled three identical VCOs. The third harmonic signal of the VCO is extracted and enhanced, and the PLL only needs to work at the fundamental frequency. Nevertheless, the drawbacks of using N-push VCOs include a larger chip area, low output power, low-energy efficiency, and performance degradation due to mismatches among *N* VCOs. As illustrated in Fig. 24(d), Zong *et al.* have demonstrated a 60 GHz frequency generator on top of a 20 GHz VCO and an implicit multiplier in [120]. This design boosts the third-harmonic based on a transformer-based dual-tank resonator topology and further filters and extracts it using a three-stage power amplifier. Injection locking (IL) techniques for mmWave frequency synthesizer designs [62], [121], can provide competitive performance such as tuning range and phase noise. A recent work of 5G LO generation is based on

injection-locked frequency multiplier (ILFM) and frequency-tracking loop (FTL) [122]. Its LO plan enables a very wide frequency coverage from sub-GHz to 30 GHz for multi-band applications required for 5G and 3GPP legacy standards. As illustrated in Fig. 25, a fractional-N PLL frequency synthesizer generates a carrier signal from 2.7 to 4.2 GHz, which is further divided by 4 to serve the sub-GHz cellular bands, such as LTE low bands. Moreover, it can be divided by 2 to generate LTE mid-low bands and LTE mid bands. In addition, after being divided by 2 and multiplied by various injection-locked frequency multipliers (ILFMs), all cellular bands of interest can be obtained with good integrated phase noise. Such a 5G LOs prototyping design might be a suitable candidate for 5G mobile devices as it can simultaneously provide multiple bands to facilitate 5G-LAA and 5G Super-CA applications.

G. BASEBAND SIGNAL PROCESSING
1) SYSTEM AND ALGORITHMS
With the hybrid beamforming architecture used at the UE end, some part of the signal processing functions are performed by the baseband processing unit (BPU). Acquiring channel state information (CSI) is critical and challenging in mobile networks, and becomes more complicated for a hybrid architecture [124]. Currently, there are two dominant categories of channel estimation schemes for mmWave communications. The first one is to reduce the dimension of channel estimation problem into two steps, i.e., beam-training performed to obtain the analog precoder F_A and analog combiner W_A, effective channel matrix $W_A^H H F_A$ estimated by algorithms such as least squares. The second scheme is to exploit the sparsity of mmWave MIMO channels by directly obtaining the complete channel matrix H with low overhead [73], [125], [126]. Furthermore, after acquiring the CSI, hybrid precoding and combining need to be designed according to different hybrid MIMO architectures.

As regards enabling the cost-efficient beam training to obtain optimal F_A and W_A, there are two promising approaches. The first one is to extend the traditional single-beam training schemes that have been widely used in IEEE 802.15.3c/802.11ad (WiGig) standards [127], to multiple beams training. As illustrated in Fig. 26, the codebook based single-beam training protocol usually contains
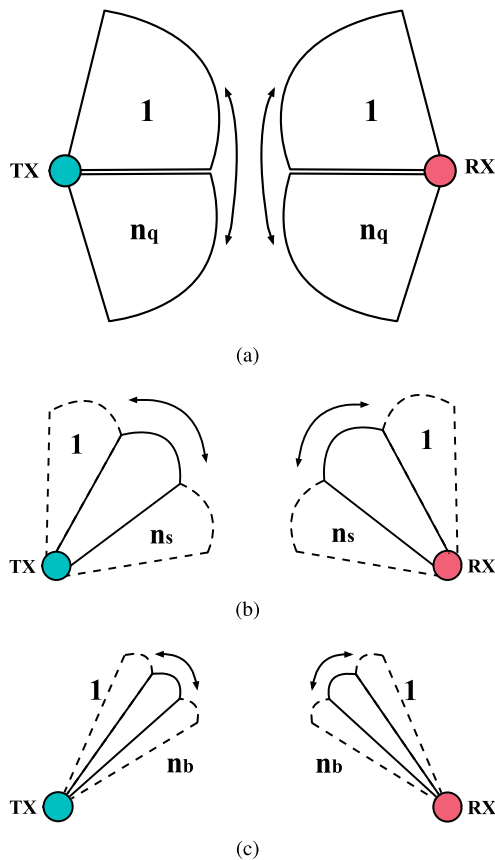
FIGURE 26. Three phases of codebook based beam training (a) quasi-omni pattern training, (b) sector level training, and (c) beam-level searching.

three stages: quasi-omni pattern training, sector-level searching, and beam-level searching. Compared to the iterative method [128], the codebook based beam training experiences the lowest training duration. In [129], a novel beamforming protocol called multiple sector ID capture (MIDC) is proposed for 60-GHz communication to improve the precision of detecting the best link via considering the imperfection of Q-omni patterns. Furthermore, this hierarchical search can be applied to hybrid architecture in which the wide beam can be designed without reducing the transmit power [130]. The second approach for beam training is to use algorithms developed from machine learning techniques [131]–[135].

Regarding the hierarchical codebook design, authors of [136] proposed two basic criteria and devised an efficient complete binary-tree structured hierarchical codebook by jointly using sub-array and deactivation antenna processing techniques, with superiority shown over existing alternatives. Moreover, a principal component analysis (PCA)-based broadband hybrid precoder/combiner design for mmWave massive MIMO was investigated in [137]. A low-dimensional frequency flat precoder/combiner from the optimal frequency-selective precoder/combiner was designed for full-connected array, with further extension to the partially connected sub-array given the antenna

grouping pattern. Moreover, a shared agglomerative hierarchical clustering (shared-AHC) was proposed and inspired by cluster analysis in the field of machine learning.

2) CIRCUITS AND IMPLEMENTATION

Linear processing in hybrid massive MIMO is favored for providing competitive precoding and detection performance, but it does not guarantee low computational complexity due to large matrices operations [138]. However, processing latency is a crucial design consideration particularly for high-mobility application scenarios. For example, in order to cope with a mobility of 70 km/h, the precoding turnaround time is controlled to 0.15 ms [139]. Moreover, beam management including beam searching, beam tracking and beam alignment may make it more challenging for the precoding/combining latency. Therefore, a suitable beamformer structure (at both BS and UE ends) facilitating direction (AoA/AoD) learning is required for initial UE discovery [140].

Regarding the practical circuits and systems design, it is envisioned that 2G/3G/4G/5G sub-6 GHz modems and a 5G mmWave dedicated modem could be separated due to the characteristic differences in carrier frequency, waveform, modulation scheme, multiple access (MA) scheme, etc. Correspondingly, the designs of the baseband digital front end (BB DFE), MIMO detector, channel estimator, channel coder/decoder, PA power supply modulators, can be highly customized.

As early as 2015, a hybrid RF/baseband precoding processor based on parallel-index-selection matrix-inversion-bypass (MIB) simultaneous orthogonal matching pursuit (OMP) for mmWave MIMO system was proposed and implemented using TSMC 90-nm CMOS process [141]. Via applying the MIB-OMP algorithm to the precoder/combiner reconstruction and proposing a new iterative residual update procedure, the computation complexity is reduced with minimized BER performance degradation. When operating at 167 MHz with 243.2 mW power consumption, the processor achieved 4 M, 4.9 M, 6.7 M, and 6.7 M channel matrices per second in 4, 3, 2, 1-stream modes, respectively.

Later in [142], a 128×8 ($M \times K$, M is the number of antennas, and K stands for the number of users) massive MIMO precoder-detector is designed in 28-nm FD-SOI process. Zero-forcing (ZF)/minimum mean-squared-error (MMSE) is employed for uplink detection, with an energy efficiency of 60 pJ/b at 300 Mb/s detection rate. For downlink precoding, adaptive QR-decomposition (QRD) algorithm is adopted, a 300 Mb/s precoding data-rate is achieved with an energy efficiency of 6.56 nJ/QRD. Furthermore, in 2018, a 128×16 link-adaptive near-optimal massive MIMO detector based on expectation propagation detection (EPD) for upto 256-QAM is implemented in 28-nm FD-SOI process [143]. With 1.8 Gbps system throughput and an energy efficiency of 70 pJ/b, the EPD outperforms a linear MMSE detector in both non-line-of-sight (NLOS) and line-of-sight (LOS) conditions.
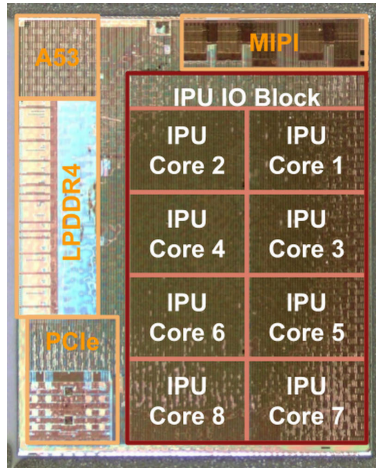
FIGURE 27. Google Pixel Visual Core (PVC) chip photo [147].

As the energy efficiency of massive MIMO pre-ocder/detector/processor will be steadily advancing, batter-powered mobile user equipments can be equiped with more cost-efficient 5G (and beyond) cellular baseband processor to further improve the UE wireless performance.

In regards to the MAC layer design, algorithms for LTE-LAA [144], 5G-LAA, 5G Super-CA and mode-switching functions, will be implemented to facilitate energy-efficient application-centric operations. For example, some effective LBT based MAC protocol [144] for 4G needs to be extended for a 5G-LAA system. Furthermore, spectrum sensing will be crucial to effectively deal with 5G Het-Net and dynamic environments. Therefore, some cooperative spectrum sensing algorithms based on machine learning techniques [145] may significantly increase the detection probability; accordingly, the quality of experience (QoE) and QoS are also improved.

H. DEEP LEARNING ON MOBILE DEVICES
Noticeably, deep learning hardware has recently been enabled into the user equipment devices in various ways. For example, the so-called ''intelligent machines'', Huawei Mate 10, has employed a dedicated neural network processing unit (NPU) in the Kirin 970 SoC [146], to enhance AI-related tasks, such as camera recording, voice recognition and assistance, object recognition, memory and storage management. Google has released the Pixel Visual Core (PVC), which is its first custom-designed co-processor for consumer products. It has been integrated into Google Pixel 2 to handle the most challenging imaging and machine learning applications [147]. As illustrated in Fig. 27, there are 8 image processing unit (IPU) cores, each of which contains 512 arithmetic logic units (ALUs). According to [147], using PVC, high dynamic range (HDR+) can run 5 times faster and at less than one-tenth the energy than running on the application processor (AP).

The 64-bit ARM-based SoC, Apple A11 Bionic, has included a neural network hardware called ''neural engine'' [148] which can be used for the machine learning

tasks such as Face ID (on iPhone X/XS) and Siri (intelligent personal assistant). This revolution has enabled implementing deep learning solutions from a cloud-based approach to an on-device one [149], which is particularly effective in protecting user privacy through bypassing.

The fast-booming deep learning/machine learning techniques can also dramatically benefit wireless communications to obtain a higher performance gain. In addition to the previously discussed applications, machine learning/deep learning techniques can be also extensively applied to, channel estimation [150], beam training [133], indoor localization [151], radio frequency fingerprinting [152], scheduling beamforming [153], predicting the network traffic, performing spectrum sensing in HetNet, learning user habits, device-free wireless localization [154], WiFi imaging [155] and its applications in device-free fall detection [156]. These techniques will greatly improve the comprehensive performance of a 5G and beyond UE device.

VI. 5G AND BEYOND UE WIRELESS AND PRODUCT DESIGN AND FUTURE TRENDS
Contemporary mobile user equipment becomes more complicated than ever, which needs to consider both engineering performance and aesthetics in product design. This is more so in future 5G and beyond UE design. On one hand, the 3GPP legacy and new standards should be implemented altogether with other wireless communications standards including WiFi, while on the other hand, the user experience which is partly associated with product design needs to be well sustained.

A. ANTENNA AND PRODUCT CO-DESIGN
1) As one critical feature, high-order MIMO antennas for sub-6 GHz applications need to be enabled on UE. In [157], 8×8 MIMO antennas working at 3.4-3.6 GHz, together with 4G 2×2 MIMO antennas operating at 824-960 MHz and 1710-2690 MHz, are presented with satisfactory antenna efficiency and channel capacity. In order to achieve high port isolation between antenna elements, antenna decoupling techniques have been developed in recent years such as current traps [157] and neutralization lines [158], [159]. They may also become instrumental for future 5G mobile antennas and particularly valuable for the UE design.

2) As proposed and illustrated in Fig. 28, we envision that 5G sub-6 GHz antennas, 5G mmWave/WiGig beam-forming (BF) modules, and antennas used for other wireless technologies can coexist harmoniously with suitable design techniques and arrangement. Ant1 and Ant2 form 4G 2×2 MIMO antennas that are demonstrated in [157], and they are placed on top part of the 5G UE. Moreover, a neutralization line (NL) colored in blue is used for enhancing the isolation. Ant3-10 from [157] are proposed for 5G sub-6 GHz applications such as 3400-3600 MHz band, and they can be extended for higher bands and multi-band
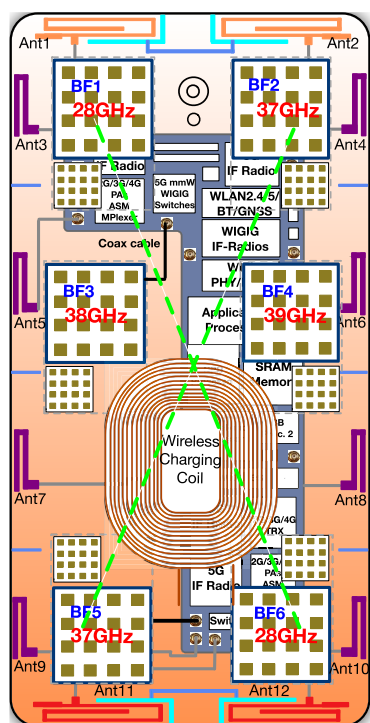
FIGURE 28. 5G UE (smartphone) wireless system and product co-design back transparent view, and 5G mmWave carrier aggregation configuration.
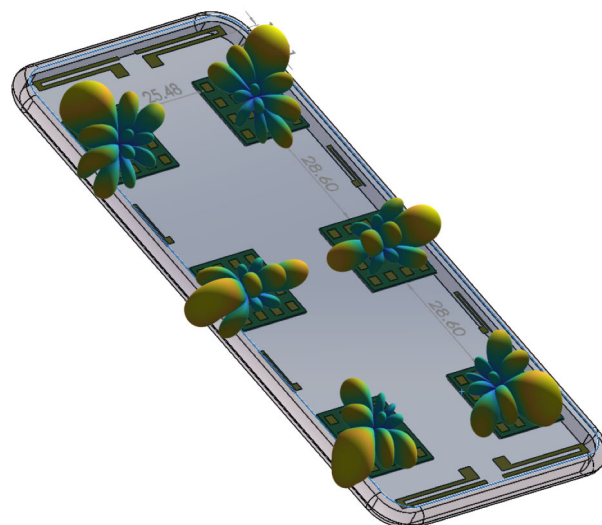
FIGURE 29. Wireless communication and product co-design example with six 28-GHz beamforming modules activated and simulated radiation pattern visualized.

applications as well, e.g., for example, above 4 GHz. In order to improve the antenna isolation, a NL that is also colored in blue is proposed to be inserted between these antenna elements. On the bottom part of 5G UE, similar 4G 2×2 antennas are situated.

3) After packing sub-6 GHz antennas, there remains approximately 70% effective area that is assigned to mmWave BFMs. First, BF modules BF1-6 have integrated the extra WiGig antenna arrays operating from 57-71 GHz since we assume that a high-performance wideband antenna array operating directly from 28-71 GHz may not be immediately available from the market.

4) Considering the antennas and BF modules interface, all sub-6 GHz antennas are directly connected to the MLB. 5G mmWave/WiGig BF modules are accommodated in the rear housing and connected to the 5G cellular IF-Radios and WiGig IF-radios, respectively. Furthermore, the "5G Cellular/WiGig Mode Switches" are implemented on the MLB and should be situated close enough to 5G cellular IF-Radios and WiGig IF-Radios.

5) As illustrated by another design instance in Fig. 28, the entire UE (smartphone) wireless and product co-design stacks up the wireless hardware by several layers (in the order from top to bottom counted from back housing case). The first layer on top contains BF modules, sub-6 GHz antennas, and antenna interface (cables); a Qi-compliant [160] wireless charging coil is situated in the same layer as 5G antennas/arrays, and it normally operates at 110 to 205 kHz [161]. As noted,

since the transmission distance is inversely proportional to the charging efficiency [162], the thickness of BF module should be minimized with an estimated value is 1.5 mm according to [26]. The MLB is assigned to the second layer which accommodates the battery, data/charging connector and other gadgets. Moreover, camera and 3D sensor modules, may occupy both the first and second layer of the UE. Finally, the third layer beneath the MLB and battery is the placement of the metallic screen bracket which blocks the antenna radiation and enhances the signal integrity [26], [33].

6) Particularly, regarding the rear case (antenna back housing), metallic (alloy) material that has been popularly used may face some changes. If mmWave beamforming is adopted, without conducting special engineering processing [66], [163], metallic rear case can largely affect the performance of phased arrays in its near-field distance, unless (antenna) notch cut/slots are properly designed for BF modules [164]. Fortunately, some alternative materials have been put into successful applications. For example, Xiaomi's Mi MIX smartphone is manufactured with a ceramic rear case [165], which is costly but has advantages in heat dissipation, hardness level, and causing less microwave penetration loss. Other material includes tempered glass that is used on products such as iPhone 8, iPhone X/XS, and Google's Pixel 3. Applying new materials helps exert to enhance the RF performance of mmWave BF modules.

B. CONFIGURING AND OPERATING SCHEMES OF WIRELESS UE SYSTEM

1) The 6 BF modules in the DPA-MIMO architecture are configured to work at various modes. For example, they can co-work at the same carrier frequency to enable

at least 6 independent spatial streams. The challenge lies in that, AoD and AoA should be well controlled and the beams need to be rapidly and precisely tracked and aligned in order to lower the interference (or increase the spatial filtering). The spatial multiplexing gain in a DPA-MIMO system is highly associated with the envelope correlation coefficient (ECC) that is used to index the independence of two antennas (arrays)' radiation patterns. In order to minimize the ECC, there are generally three methods, first, polarizing adjacent mmWave BF modules; second, increasing the separation among BFMs; third, making peak radiation direction distinct. Through designing a real-world smartphone rear housing case in SolidWorks (CAD tool) with 28 GHz BF modules (16-element) and sub-6 GHz antennas embedded, we visualize the entire UE device with the simulated radiation patterns as shown in Fig. 29. The minimum edge-to-edge spacing of BF modules is controlled to more than 2.3 free-space wavelengths, moreover, the main lobes are steered to distinct direction to reduce the ECC.

2) Nevertheless, the aforementioned beam management scheme presents a huge challenge to both UE and BS designs, although these designs are conditionally implementable in some application scenarios. Another alternative DPA-MIMO configuration, as presented in Fig. 28, is proposed to assign neighboring BF modules with different frequency bands. Any two BF modules operating at the same frequency band, are situated from each other by abundant (diagonal distance as marked in green dash lines) isolation to obtain an optimized spatial multiplexing gain (2 layers). This can be treated as a frequency-space division (FSD) operation mode of a DPA-MIMO system; consequently, in-band interference can be minimized.

3) Based on the FSD mode, the wireless communication within a 5G HetNet is depicted in Fig. 30. A UE device enables two mmWave BF modules to communicate with indoor WiFi (WiGig) router, while a cellular base station simultaneously communicates with the indoor UE through activating another four spatial beams. Through enabling carrier aggregation of both cellular and WiFi, an extremely high speed can be obtained to cope with more challenging application scenarios.

4) Fig. 31 further illustrates an example UE when 5G Super-CA mode is activated when BF1-6 operate at 28 GHz, 37-39 GHz, and WiGig (60/62/64/66 GHz) bands, respectively. This mitigates the in-band interference and boosts up the spatial multiplexing gain. Moreover, antennas Ant1, Ant2, Ant11, and Ant12 operate at sub-3 GHz bands to support a 4-layer MIMO, while Ant3-10 work at 3-6 GHz bands with 8-layer MIMO supported. Theoretically, according to the definition of UE FoM in [26], more aggregated carriers and higher
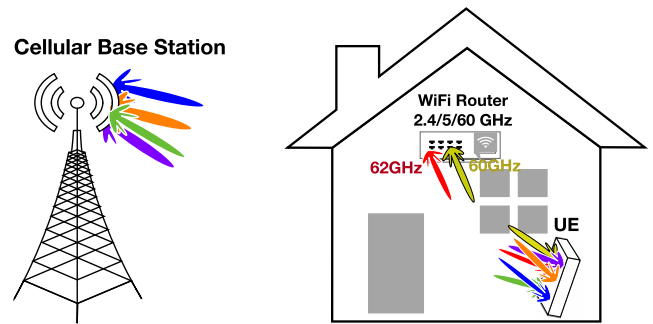

FIGURE 30. Application scenario of 5G HetNet where cellular and WiFi (WiGig) carrier aggregation is enabled in high bands.
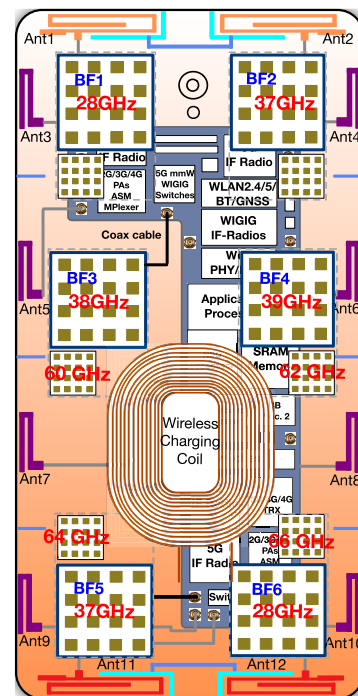

FIGURE 31. Cellular and WiGig super carrier aggregation (Super-CA) configuration of DPA-MIMO enabled 5G UE (smartphone) system.

peak data rates can generate a better figure of merit performance of a UE device.

5) Fig. 32 demonstrates the generic process of initializing the communication for the DPA-MIMO based user equipment. First of all, channel estimation will be performed through beam training such that the corresponding systematic strategies and behaviours will take place, such as handling the situation when the BF module(s) is(are) blocked. Moreover, the algorithms related to hybrid beamforming will be managed in this phase.

6) On the other hand, Fig. 33 describes a process of operating a multiplexed DPA-MIMO based wireless communication system, which comprises of several steps: spectrum sensing, determining network availability, examining application requirement, network selection,
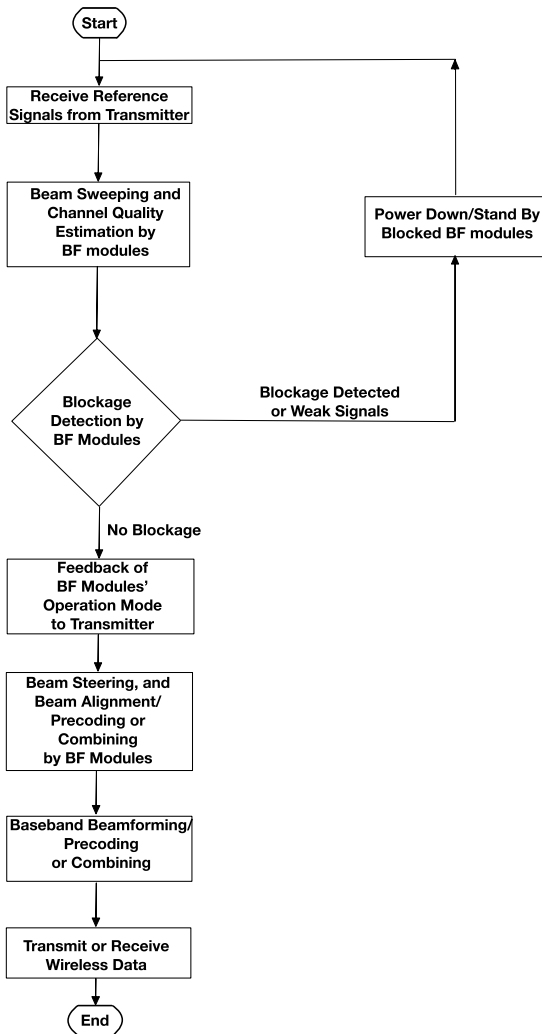
FIGURE 32. Flow chart of beam management and communication initialization in a DPA-MIMO enabled wireless communication system.
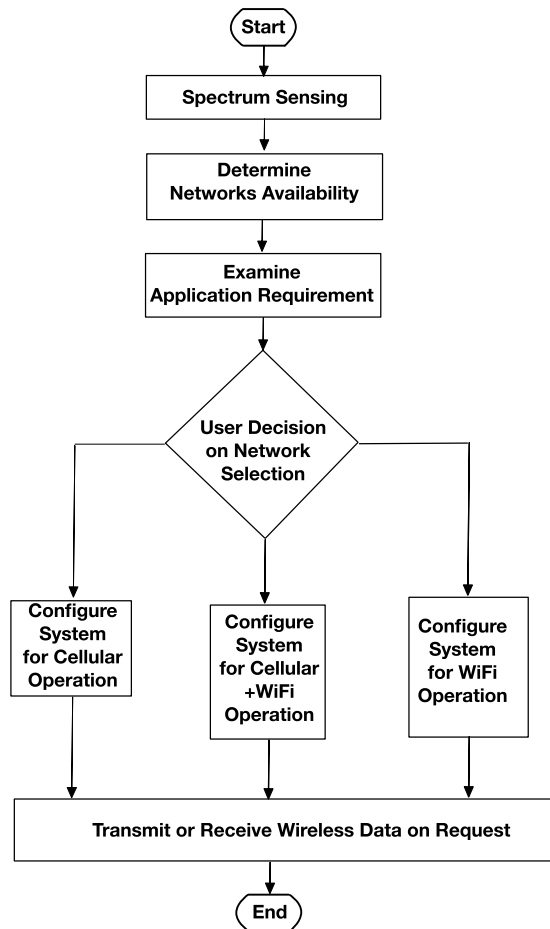

FIGURE 33. Flow chart of multiplexed DPA-MIMO wireless communication in a user equipment device.

configuring cellular operation, configuring cellular and WiFi (5G-LAA, or 5G-Super CA) operation, and configuring WiFi operation. More complex and specific algorithms need to be built and expanded on this flow chart to enable cost-effective PHY-MAC cross-layer designs.

7) Regarding whether DPA-MIMO works at standalone spatial multiplexing mode (N_{BF} independent spatial streams over the same band) or FSD mode shown in Fig. 28, it depends on the specific application scenario described earlier and many other conditions such as channel status, speed/latency requirements, etc. Therefore, energy-efficient MAC protocols and MAC-PHY co-design can facilitate a high-performance 5G and beyond UE.

To summarize here, the increasing resource handling capabilities and higher complexity of 5G and beyond hardware at the UE end will unavoidably result in higher power consumption. However, the energy efficiency (joule/bit) of wireless communications can be significantly improved when a larger bandwidth is aggregated via using 5G bands. With this being said, a 5G UE can transmit/receive the same amount of data, using less time and energy, compared to its 4G counterparts. The second complication lies in higher cost of mass production, which includes UE prototype design and verification, supply chain and quality control, etc. It should be noted that this cost increment will be moderated over time as productivity is improved.

C. PROOF-OF-CONCEPT DESIGN AND FIELD TEST

In order to verify the aforementioned wireless-product co-design concept, 5G proof-of-concept based on distributed phased arrays is illustrated in Fig. 34. Together with wireless charging coil, four mmWave BFMs operating at WiGig frequency bands are accommodated in the rear case made of ceramic material (e.g., aluminum nitride (AlN)) which can facilitate the heat distribution and minimize the penetration loss at mmWave bands when compared with rear cases made of metallic alloy and tempered glass.

As shown in Fig. 34(a), two BF modules (2×8 antenna array on each) are placed alongside the top frame with an

(a)   (b)
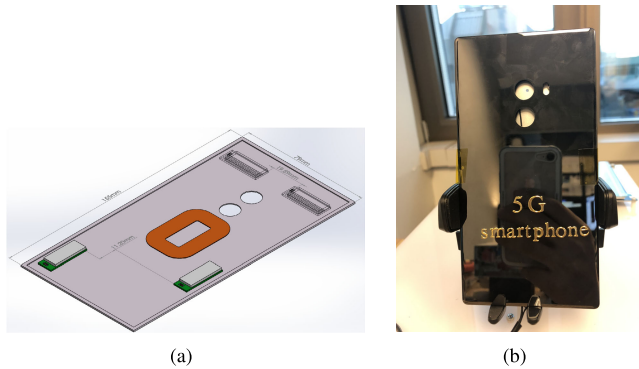
FIGURE 34. 5G user equipment PoC (a) wireless-product co-design manifestation and (b) prototype for field tests.

(a)

(b)

FIGURE 35. Foldable smartphones announced at MWC 2019. (a) Samsung Galaxy Fold [167] and (b) Huawei Mate X [168].

edge-to-edge spacing of around 4 times the free-space wavelength at 60 GHz. Such large spacing can minimize the ECC to mitigate the spatial filtering. Furthermore, another two BF modules placed on each side of the bottom part of the housing are perpendicular to the top two BF modules to minimize radiation coupling, with a vertical edge-to-edge spacing of 11 mm (> 2 times free-space wavelength) between each other. All BF modules are connected through RF coaxial cables to the IF-radio blocks, baseband processors, and eventually the application processors.

Field tests were conducted for two representative channel models [166], i.e., Indoor Hotspot (InH)-Office (corridor) and Urban Micro (UMi)-Street Canyon. With a 21 dBm EIRP each BF mdoule is capable of transmitting at 60 GHz, the peak downlink speed is measured at 4.23 Gbps and 4.16 Gbps, while the speed decreases to 2.88 Gbps and 2.71 Gbps at a distance of 20 meters, for InH-Office and UMi-Street Canyon, respectively.

D. NEW AND FUTURE TRENDS IN WIRELESS UE DESIGN
The technological advances and evolution outside the domain of wireless design, have also been shaping the future UE. For example, at Mobile World Congress (MWC) 2019 Barcelona, Samsung and Huawei both announced their own foldable mobile devices, i.e., Samsung Galaxy Fold, and Huawei Mate X, as illustrated in Fig. 35. One of the most critical enablers is the organic light-emitting diode (OLED) display technology, which has several advantages over its counterpart, liquid crystal display (LCD), particularly for the mobile UE design. For example, unlike LCD [169] which requires bulky backlight and filters, an OLED screen contains a thin film of organic compounds that produces light from an electric current right at the surface of the device [170], which makes OLED lighter, thinner and flexible, and thus ideal for the foldable UE design with a slim form factor.

The foldable UE design facilitates more hardware area and therefore accommodates more antennas and mmWave beamforming modules. As depicted in the proposed DPA-MIMO based foldable UE design in Fig. 36, there are totally 12 beamforming modules and 20 sub-6 GHz antennas that
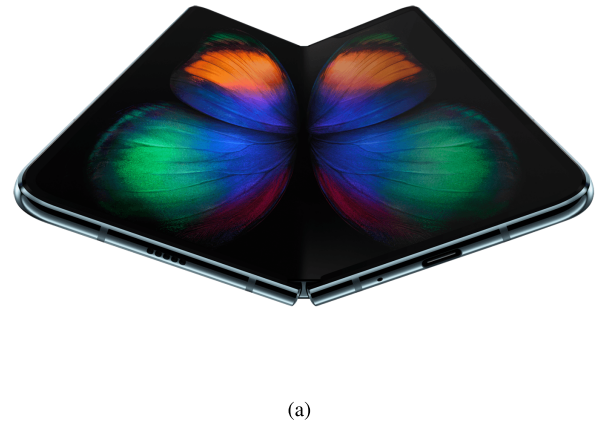
can enable more powerful and diverse Super-CA combinations with higher data throughput and better spherical coverage indexed by coverage efficiency. Moreover, the 5G and beyond UE may take diverse forms. For example, wearable devices such as virtual reality and mixed reality devices [171], [172], satellite communications (other than GNSS) supported devices, can be shaped and enhanced by 5G and beyond technologies.

E. ENABLING TERAHERTZ TECHNOLOGIES INTO USER EQUIPMENT?
Terahertz technology has been explored by many technology pioneers for several decades now. Due to the non-ionizing radiation and low photon energy features, THz radiation can penetrate fabrics, plastics, and living tissue with some depth without causing damage. Therefore, THz radiation has been conventionally applied to several research domains, namely, medical imaging, chemical imaging [173], security screening, materials sensing, planetary exploration [174], molecules spectroscopy [175], astronomy [176], pharmacology.

In recent years, more promising THz related technologies and applications have been developed. For example, [177] demonstrated a fully-electronic clock using sub-terahertz
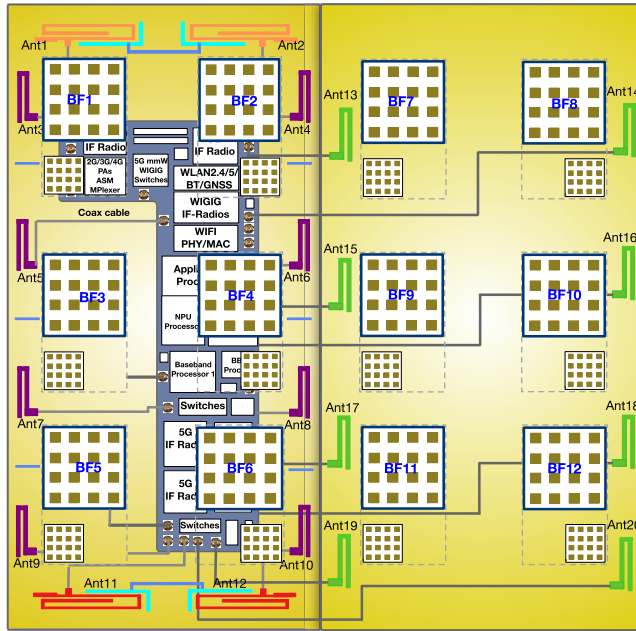
FIGURE 36. DPA-MIMO enabled cellular and WiFi co-design example in a foldup smartphone.

FIGURE 37. Specific attenuation from 0.1 to 1 THz for several atmospheric conditions based on ITU-R models.

rotational spectroscopy as an alternative to previous miniature clocks; in [178], continuous-wave radiation at 0.4 THz was generated to uniformly illustrate various input projects of the 3D-printed diffractive deep neural network (D^{2}NN). Reference [179] investigated THz Interconnect (TI) applications (for inter-/intra-chip communications) via utilizing the THz frequency spectrum sandwiched between microwave and optical frequencies with the advantages of both electronics and optics leveraged.

Although THz waves are appealing to 6G wireless communications due to unallocated large spectrum, the atmospheric attenuation because of molecular absorption is much larger and more significant than the microwave frequency bands [15], [180]. Based on the ITU-R attenuation by atmospheric gases models [181], specific attenuation (dB/km) over frequency range from 0.1 to 1 THz is simulated and plotted in Fig. 37 for several meteorological conditions (under sea-level altitude, atmospheric pressure of 1013.25 hPa and temperature of 20°), namely, dry air, air with water vapour density of 7.5g/m^3, medium fog, heavy fog, moderate rain (5 mm/h), heavy rain (25 mm/h), and violent rain (100 mm/h). It is observed that, H$_2$O molecule can introduce significant attenuation to the frequencies of interest, although the attenuation may vary according to the specific type of meteorological conditions. As a result, THz outdoor communications can be highly constrained and subject to additional loss due to weather conditions, while THz indoor communications may be more immune to this challenge. From this aspect, the beamforming and phased array technologies are favored in THz systems.

Furthermore, the THz reflection properties are also different than GHz. Take indoor communication environments
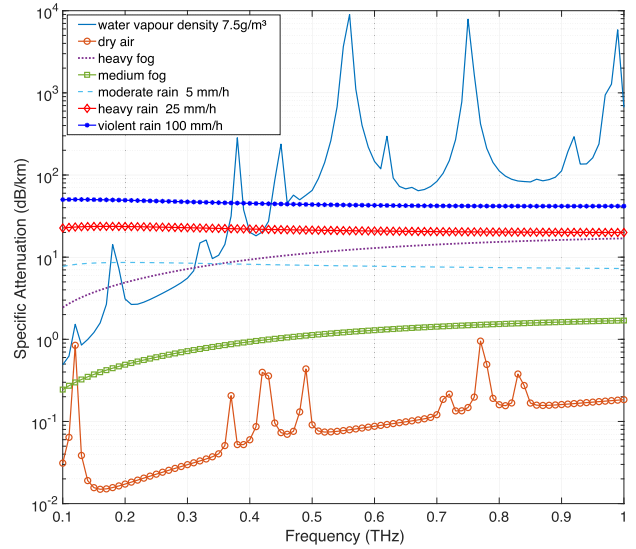
for example, the surface variations of many indoor objects are comparable to the THz wavelength (300 μm to 3 mm), therefore, smooth surfaces regarded for GHz become rough ones for THz [15]. The roughness factor is

$$\rho = (\rho_0 + \rho_1)e^{-g/2} \tag{13}$$

with

$$g = \left(\frac{2\pi \cdot \Delta \cdot (cos\theta_1 + cos\theta_2)}{\lambda} \right)^2, \tag{14}$$

where ρ_0 represents the scattering coefficient corresponding to the specular reflection while ρ_1 denotes the corresponding one due to the diffusely scattered field. Δ is the roughness deviation, θ_1 and θ_2 are incident and reflection angles, respectively. When g $\geq$ 1, the surface is moderately rough; then, g $\gg$ 1, the surface is very rough. Furthermore, the angular spreads at THz frequencies are larger than at GHz due to the rough surface, which means the antennas at TX can be smaller than $\lambda_0/2$ for a THz MIMO system [15]. As a result, more THz MIMO antennas can be accommodated on the same area.

With respect to the THz system implementation, driven by the rapid advancement of IC processes and design techniques, THz circuits and systems can be realized at the semiconductor level, which makes the THz imaging systems downsized and more compact. With high-speed SiGe HBT technology achieving the next technology node at 700 GHz f_{max} [182], SiGe HBT technology is capable of enabling circuits fundamentally operating above 300 GHz [183].

As early as 2012, [184] demonstrated a 144 GHz subcarrier synthetic aperture radar (SAR) phase radar designed in 65-nm CMOS for 3D imaging. The radar is able to achieve a spatial resolution and depth resolution of 3.3 cm^2 and 7.6 mm over 1-m distance, respectively, with only 457-mW

(a)

(b)
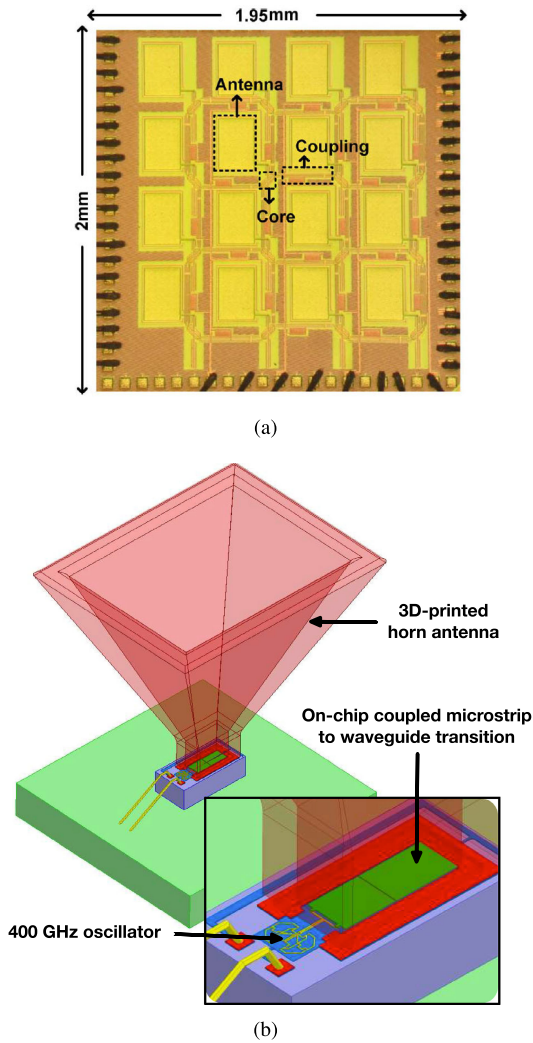
FIGURE 38. (a) Chip micro photo of 2-D phased array designed and fabricated in 65-nm bulk CMOS process with on-chip antennas [69], and (b) 400 GHz transmitter chip with 3D-printed high-gain horn antenna [187].

total power consumption for both TX and RX ends. Reference [185] presented a 65-nm CMOS 1k-pixel THz camera working from 0.7 to 1.1 THz to collect all source-pixel beams, with high energy efficiency and a minimum noise equivalent power (NEP) at 100 pW/$\sqrt{\text{Hz}}$. Reference [186] presented a very low-noise 183 GHz CMOS/In-P-hybrid heterodyne spectrometer system that detects H_2O and CH_3CN molecules, for NASA's stratospheric balloon platform. Standaert and Reynaert presented 400 GHz transmitter and receiver chips designed in a 28-nm bulk CMOS process in [187]. This work demonstrated direct transition techniques between a THz chip and a waveguide, which provided a flexible low loss interface. Moreover, a 3D-printed high-gain pyramidal horn antenna is aligned and placed on top of the THz chip, eliminating the need of a bulky silicon lens [188] for the imaging system.

More recently, the mmWave coalition has been proposing rules for commercialization of fixed and mobile systems above 95 GHz in order to create a global ecosystem [189].

There are over 21 GHz contiguous bandwidth from 95 to 275 GHz. This makes THz bands technologies for next-generation wireless systems (6G) targeting 100 Gbps and higher speed, although there are many challenges to overcome, such as large losses with a combination ohmic losses and dielectric losses from substrate coupling [179]. As early as 2017, [20] demonstrated the world's first 300 GHz CMOS transmitter achieving 105 Gbps; [190] designed a 300 GHz, 100 Gbps wireless transceiver using monolithic microwave integrated circuit (MMIC) process; then in 2019, [191] presented a single-chip CMOS transceiver with 80 Gbps data throughput at 300 GHz.

It is worth investigating the THz antenna design and integration technologies for future 6G UE systems. The reduced footprint of THz antennas makes on-chip antenna designs more popular with benefits such as easier on-chip impedance matching [80], less interface loss due to conventional bondwires, bondpads and PCB that introduce significant attenuation for THz signals due to the parasitic inductance and capacitance. As illustrated in Fig. 38(a), a 2-D phased array designed and fabricated in a 65-nm bulk CMOS process with on-chip antennas is able to provide a 95° beam steering and peak EIRP at 17.1 dBm, from 337 to 339 GHz [69].

However, the silicon substrate in general is not suited for on-chip antennas fabrication due to low resistivity and high dielectric constant [80]. Therefore, some special but perhaps more expensive process and design techniques need to be used to enhance the on-chip antenna performance. For example, in order to improve the radiation efficiency, authors in [192] used a $\lambda/4$-thick quartz superstrate on top of the microstrip antenna working at 360–400 GHz, which increased the antenna peak gain and the peak efficiency by 3.1 dB and 3.5 dB, respectively. Moreover, artificial magnetic conductor (AMC) were reported to enhance the on-chip antenna efficiency for both mmWave [86] and THz applications [193].

As highly possible to be adopted in 6G, on-chip antennas and phased array design can facilitate high-performance beamforming techniques. The beam tracking and training are more complicated and challenging to implement as the number of phased array antennas may be larger than its 5G mmWave counterpart.

In addition, a compact THz system solution in [187] is enabled by assembling and integrating a 3D-printed horn antenna on top of the THz chip as shown in Fig. 38(b). The THz transmitter is coupled through a differential patch antenna coupler to the horn antenna with a small build volume of only about 3 × 3 × 3 mm, with a realized gain of the total transition from the oscillator output on wards being 14 dB. Such an alternative THz antenna system design method can facilitate a 6G hand-held device with a small form factor.

Based on emerging technologies and trends, it is envisioned that the commercial THz chipsets and hardware solutions that are suitable for various applications at the user equipment end may be available for the next decade.

VII. CONCLUSION

Multi-standard, multi-function user equipment design for 5G and beyond, e.g., 6G, has triggered broad and urgent attention. In this paper, we have investigated recent 5G focused technologies such as carrier aggregation techniques and spectrum sharing paradigms, and classified future typical 5G and beyond application scenarios enabled by 5G LAA and 5G Super-CA.

The proposed DPA-MIMO based multiplexing and reuse architecture has been shown to facilitate a cost-effective and energy-efficient 5G and beyond UE design to cope with various existing and potential 5G deployment scenarios. Furthermore, in order to evaluate and predict the cellular and WiFi co-enabling solutions, the cutting-edge hardware design techniques and state-of-the-art design examples have been investigated. Examples of wireless modules hosted in a UE product have led to conceptual designs for antenna placement, DPA-MIMO configurations and frequency-space division of BFMs. These enabling technologies and their further evolution will pave the way to more diversified and more powerful multi-functional user equipment.

Moreover, a proof-of-concept UE product design based on 60 GHz commercial chipsets and its field test results have been presented to validate the design ideas in this paper. Finally, the recent progress of smartphone design and the THz technologies have been reviewed and discussed as important elements for next-generation user equipment.

ACKNOWLEDGEMENT

REFERENCES

[1] *IMT Vision—Framework and Overall Objectives of the Future Development of IMT for 2020 and Beyond*, document ITU-R M.2083-0, Sep. 2015.

[2] R. Molina-Masegosa and J. Gozalvez, "LTE-V for sidelink 5G V2X vehicular communications: A new 5G technology for short-range vehicle-to-everything communications," *IEEE Veh. Technol. Mag.*, vol. 12, no. 4, pp. 30–39, Dec. 2017.

[3] S. Zhang, N. Zhang, X. Fang, P. Yang, and X. S. Shen, "Self-sustaining caching stations: Toward cost-effective 5G-enabled vehicular networks," *IEEE Commun. Mag.*, vol. 55, no. 11, pp. 202–208, Nov. 2017.

[4] M. Wollschlaeger, T. Sauter, and J. Jasperneite, "The future of industrial communication: Automation networks in the era of the Internet of Things and industry 4.0," *IEEE Ind. Electron. Mag.*, vol. 11, no. 1, pp. 17–27, Mar. 2017.

[5] S. M. Riazul Islam, D. Kwak, M. Humaun Kabir, M. Hossain, and K.-S. Kwak, "The Internet of Things for health care: A comprehensive survey," *IEEE Access*, vol. 3, pp. 678–708, Jun. 2015.

[6] T. Han, X. Ge, L. Wang, K. S. Kwak, Y. Han, and X. Liu, "5G converged cell-less communications in smart cities," *IEEE Commun. Mag.*, vol. 55, no. 3, pp. 44–55, Mar. 2017.

[7] (Dec. 2015). *5G Channel Model for Bands up to 100 GHz*. [Online]. Available: http://www.5gworkshops.com/5GCM.html

[8] Z. Gao, L. Dai, S. Han, C.-L. I, Z. Wang, and L. Hanzo, "Compressive sensing techniques for next-generation wireless communications," *IEEE Wireless Commun.*, vol. 25, no. 3, pp. 144–153, Jun. 2018.

[9] M. Ke, Z. Gao, Y. Wu, X. Gao, and R. Schober, "Compressive sensing based adaptive active user detection and channel estimation: Massive access meets massive MIMO," 2019, *arXiv:1906.09867*. [Online]. Available: https://arxiv.org/abs/1906.09867

[10] M.-A. Russon. (Apr. 2017). *US and South Korea Just Performed the World's First Live 3D Hologram Call Over 5G*. [Online]. Available: http://www.ibtimes.co.uk/us-south-korea-just-performed-worlds-first-live-3d-hologram-call-over-5g-1615957

[11] Z. Xiao, P. Xia, and X.-G. Xia, "Enabling UAV cellular with millimeter-wave communication: Potentials and approaches," *IEEE Commun. Mag.*, vol. 54, no. 5, pp. 66–73, May 2016.

[12] Y. Huo and X. Dong, "Millimeter-Wave for unmanned aerial vehicles networks: Enabling multi-beam multi-stream communications," 2018, *arXiv:1810.06923*. [Online]. Available: https://arxiv.org/abs/1810.06923

[13] *Report and Order and Future Notice of Proposed Rulemaking*. Accessed: May 29, 2019. [Online]. Available: https://apps.fcc.gov/edocs_public/attachmatch/FCC-16-89A1.pdf

[14] C. Wang, B. Lu, C. Lin, Q. Chen, L. Miao, X. Deng, and J. Zhang, "0.34-THz wireless link based on high-order modulation for future wireless local area network applications," *IEEE Trans. THz Sci. Technol.*, vol. 4, no. 1, pp. 75–85, Jan. 2014.

[15] Z. Xu, X. Dong, and J. Bornemann, "Design of a reconfigurable MIMO system for THz communications based on graphene antennas," *IEEE Trans. THz Sci. Technol.*, vol. 4, no. 5, pp. 609–617, Sep. 2014.

[16] C. Lin and G. Y. Li, "Indoor terahertz communications: How many antenna arrays are needed?" *IEEE Trans. Wireless Commun.*, vol. 14, no. 6, pp. 3097–3107, Jun. 2015.

[17] N. Khalid and O. B. Akan, "Experimental throughput analysis of low-THz MIMO communication channel in 5G wireless networks," *IEEE Wireless Commun. Lett.*, vol. 5, no. 6, pp. 616–619, Dec. 2016.

[18] Y. Zhao, Z.-Z. Chen, Y. Du, Y. Li, R. Al Hadi, G. Virbila, Y. Xu, Y. Kim, A. Tang, T. J. Reck, and M.-C. F. Chang, "A 0.56 THz phase-locked frequency synthesizer in 65 nm CMOS technology," *IEEE J. Solid-State Circuits*, vol. 51, no. 12, pp. 3005–3019, Dec. 2016.

[19] X. Li, J. Yu, K. Wang, M. Kong, W. Zhou, Z. Zhu, C. Wang, M. Zhao, and G.-K. Chang, "120 Gb/s wireless terahertz-wave signal delivery by 375 GHz-500 GHz multi-carrier in a 2 × 2 MIMO system," in *Proc. Opt. Fiber Commun. Conf. Expo. (OFC)*, San Diego, CA, USA, 2018, pp. 1–3.

[20] K. Takano, S. Amakawa, K. Katayama, S. Hara, R. Dong, A. Kasamatsu, I. Hosako, K. Mizuno, K. Takahashi, T. Yoshida, and M. Fujishima, "A 105 Gb/s 300 GHz CMOS transmitter," in *IEEE Int. Solid-State Circuits Conf. (ISSCC) Dig. Tech. Papers*, Feb. 2017, pp. 308–309.

[21] C. S. Park, L. Sundström, A. Wallén, A. Khayrallah, "Carrier aggregation for LTE-advanced: Design challenges of terminals," *IEEE Commun. Mag.*, vol. 51, no. 12, pp. 76–84, Dec. 2013.

[22] N. Jindal and D. Breslin. *LTE and Wi-Fi in Unlicensed Spectrum: A Coexistence Study*. Accessed: May 29, 2019. [Online]. Available: https://ecfsapi.fcc.gov/file/60001078145.pdf

[23] H. Song, Q. Cui, Y. Gu, G. L. Stüber, Y. Li, Z. Fei, and C. Guo, "Cooperative LBT design and effective capacity analysis for 5G NR ultra dense networks in unlicensed spectrum," *IEEE Access*, vol. 7, pp. 50265–50279, 2019.

[24] S. Lagen, L. Giupponi, B. Bojovic, A. Demir, and M. Beluri, "Paired listen before talk for multi-RAT coexistence in unlicensed mmWave bands," in *Proc. IEEE Int. Conf. Commun. Workshops (ICC Workshops)*, Kansas City, MO, USA, May 2018, pp. 1–6.

[25] Intel. *Alternative LTE Solutions in Unlicensed Spectrum: Overview of LWA, LTE-LAA and Beyond*. Accessed: May 29, 2019. [Online]. Available: https://www.intel.com/content/dam/www/public/us/en/documents/white-papers/unlicensed-lte-paper.pdf

[26] Y. Huo, X. Dong, and W. Xu, "5G cellular user equipment: From theory to practical hardware design," *IEEE Access*, vol. 5, pp. 13992–14010, 2017.

[27] Z. Xiao, L. Zhu, J. Choi, P. Xia, and X.-G. Xia, "Joint power allocation and beamforming for non-orthogonal multiple access (NOMA) in 5G millimeter wave communications," *IEEE Trans. Wireless Commun.*, vol. 17, no. 5, pp. 2961–2974, May 2018.

[28] Z. Xiao, L. Zhu, Z. Gao, D. O. Wu, and X. Xia, "User fairness non-orthogonal multiple access (NOMA) for millimeter-wave communications with analog beamforming," *IEEE Trans. Wireless Commun.*, vol. 18, no. 7, pp. 3411–3423, Jul. 2019.

[29] Qualcomm. *Making 5G NR a Commercial Reality*. Accessed: May 29, 2019. [Online]. Available: https://www.qualcomm.com/media/documents/files/making-5g-nr-a-commercial-reality.pdf

[30] S. Chen, J. Hu, Y. Shi, and L. Zhao, "LTE-V: A TD-LTE-based V2X solution for future vehicular network," *IEEE Internet Things J.*, vol. 3, no. 6, pp. 997–1005, Dec. 2016.

[31] D. R. Pehlke and K. Walsh, "LTE-advanced pro RF front-end implementations to meet emerging carrier aggregation and DL MIMO requirements," *IEEE Commun. Mag.*, vol. 55, no. 4, pp. 134–141, Apr. 2017.

[32] L. Miller. *Carrier Aggregation Fundamentals*. Accessed: May 29, 2019. [Online]. Available: http://www.qorvo.com/resources/d/qorvo-carrier-aggregationfundamentals-for-dummies-volume-1

[33] J. Shi, A. Bettner, G. Chinn, K. Slattery, and X. Dong, "A study of platform EMI from LCD panels—Impact on wireless, root causes and mitigation methods," *Proc. IEEE Int. Symp. Electromagn. Compat. (EMC)*, Portland, OR, USA, Aug. 2006, pp. 626–631.

[34] Y. Huo, X. Dong, W. Xu, and M. Yuen, "Cellular and WiFi co-design for 5G user equipment," *Proc. IEEE 5G World Forum (5GWF)*, Silicon Valley, CA, USA, Jul. 2018, pp. 256–261.

[35] *IEEE Draft Standard for Information Technology—Telecommunications and Information Exchange Between Systems Local and Metropolitan Area Networks—Specific Requirements Part 11: Wireless LAN Medium Access Control (MAC) and Physical Layer (PHY) Specifications Amendment Enhancements for High Efficiency WLAN*, IEEE Standard P802.11ax/D4.0, Feb./Mar. 2019, pp. 1–746.

[36] Qualcomm. *CEO Steve Mollenkopf Discusses the Road to 5G at 2017 International Motor Show Germany [Video]*. Accessed: May 29, 2019. [Online]. Available: https://www.qualcomm.com/news/onq/2017/09/14/ceo-steve-mollenkopf-discusses-road-5g-2017-international-motor-show-germany

[37] K. Zhao, R. Mayzus, S. Sun, M. Samimi, J. K. Schulz, Y. Azar, K. Wang, G. N. Wong, F. Gutierrez, and T. S. Rappaport, "28 GHz millimeter wave cellular communication measurements for reflection and penetration loss in and around buildings in New York city," in *Proc. IEEE Int. Conf. Commun. (ICC)*, Jun. 2013, pp. 5163–5167.

[38] K. Haneda *et al.*, "5G 3GPP-like channel models for outdoor urban microcellular and macrocellular environments," in *Proc. IEEE 83rd Veh. Technol. Conf. (VTC-Spring)*, May 2016, pp. 1–7.

[39] A. K. M. Isa, A. Nix, and G. Hilton, "Impact of diffraction and attenuation for material characterisation in millimetre wave bands," in *Proc. Loughborough Antennas Propag. Conf. (LAPC)*, Nov. 2015, pp. 1–4.

[40] J. Ryan, G. R. MacCartney, and T. S. Rappaport, "Indoor office wideband penetration loss measurements at 73 GHz," in *Proc. IEEE Int. Conf. Commun. Workshop (ICCW)*, May 2017, pp. 228–233.

[41] M. Dano. *Editor's Corner—Verizon Says Its New Indoor/Outdoor Prototype 5G Modem Solves One of the Biggest 28 GHz Problems*. Accessed: May 29, 2019. [Online]. Available: https://www.fiercewireless.com/5g/editor-s-corner-verizon-says-its-new-indoor-outdoor-prototype-5g-modem-solves-one-28-ghz-biggest

[42] Verizon. *Verizon to Launch 5G Residential Broadband Services in up to 5 Markets in 2018*. Accessed: May 29, 2019. [Online]. Available: http://www.verizon.com/about/news/verizon-launch-5g-residential-broadband-services-5-markets-2018

[43] Y. Liu, C. Li, X. Xia, X. Quan, D. Liu, Q. Xu, W. Pan, Y. Tang, and K. Kang, "Multiband user equipment prototype hardware design for 5G communications in sub-6-GHz band," *IEEE Trans. Microw. Theory Techn.*, vol. 67, no. 7, pp. 2916–2927, Jul. 2019.

[44] J. Vieira, S. Malkowsky, K. Nieman, Z. Miers, N. Kundargi, L. Liu, I. Wong, V. Öwall, O. Edfors, and F. Tufvesson, "A flexible 100-antenna testbed for massive MIMO," in *Proc. IEEE Globecom Workshops (GC Wkshps)*, Dec. 2014, pp. 287–293.

[45] P. Harris, S. Zhang, M. Beach, E. Mellios, A. Nix, S. Armour, A. Doufexi, K. Nieman, and N. Kundargi, "LOS throughput measurements in real-time with a 128-antenna massive MIMO testbed," *Proc. IEEE Global Commun. Conf. (GLOBECOM)*, Washington, DC, USA, Dec. 2016, pp. 1–7.

[46] S. Malkowsky, J. Vieira, L. Liu, P. Harris, K. Nieman, N. Kundargi, I. C. Wong, F. Tufvesson, V. Öwall, and O. Edfors, "The World's first real-time testbed for massive MIMO: Design, implementation, and validation," *IEEE Access*, vol. 5, pp. 9073–9088, 2017.

[47] AT&T. *AT&T Launches First 5G Business Customer Trial With Intel and Ericsson*. Accessed: May 29, 2019. [Online]. Available: http://about.att.com/story/att_launches_first_5g_business_customer_trial_with_intel_and_ericsson.html

[48] K. Kibaroglu, M. Sayginer, and G. M. Rebeiz, "An ultra low-cost 32-element 28 GHz phased-array transceiver with 41 dBm EIRP and 1.0–1.6 Gbps 16-QAM link at 300 meters," in *Proc. IEEE Radio Freq. Integr. Circuits Symp. (RFIC)*, Honolulu, HI, USA, Jun. 2017, pp. 73–76.

[49] B. Sadhu *et al.*, "A 28-GHz 32-element TRX phased-array IC with concurrent dual-polarized operation and orthogonal phase and gain control for 5G communications," *IEEE J. Solid-State Circuits*, vol. 52, no. 12, pp. 3373–3391, Dec. 2017.

[50] T. Sowlati *et al.*, "A 60 GHz 144-element phased-array transceiver with 51dBm maximum EIRP and ±60° beam steering for backhaul application," in *IEEE Int. Solid-State Circuits Conf. (ISSCC) Dig. Tech. Papers*, Feb. 2018, pp. 66–68.

[51] S. Hu, F. Wang, and H. Wang, "A 28 GHz/37 GHz/39 GHz multiband linear Doherty power amplifier for 5G massive MIMO applications," in *IEEE Int. Solid-State Circuits Conf. (ISSCC) Dig. Tech. Papers*, Feb. 2017, pp. 32–33.

[52] M.-Y. Huang, T. Chi, F. Wang, T.-W. Li, and H. Wang, "A 23-to-30 GHz hybrid beamforming MIMO receiver array with closed-loop multistage front-end beamformers for full-FoV dynamic and autonomous unknown signal tracking and blocker rejection," in *IEEE Int. Solid-State Circuits Conf. (ISSCC) Dig. Tech. Papers*, Feb. 2018, pp. 68–70.

[53] S. Mondal, R. Singh, A. I. Hussein, and J. Paramesh, "A 25–30 GHz fully-connected hybrid beamforming receiver for MIMO communication," *IEEE J. Solid-State Circuits*, vol. 53, no. 5, pp. 1275–1287, May 2018.

[54] K. A. Remley *et al.*, "Measurement challenges for 5G and beyond: An update from the national Institute of standards and technology," *IEEE Microw. Mag.*, vol. 18, no. 5, pp. 41–56, Jul./Aug. 2017.

[55] W. Hong, "Solving the 5G mobile antenna puzzle: Assessing future directions for the 5G mobile antenna paradigm shift," *IEEE Microw. Mag.*, vol. 18, no. 7, pp. 86–102, Nov. 2017.

[56] K. Zhao, J. Helander, D. Sjöberg, S. He, T. Bolin, and Z. Ying, "User body effect on phased array in user equipment for the 5G mmWave communication system," *IEEE Antennas Wireless Propag. Lett.*, vol. 16, pp. 864–867, 2016.

[57] G. R. MacCartney, Jr., S. Deng, S. Sun, and T. S. Rappaport, "Millimeter-wave human blockage at 73 GHz with a simple double knife-edge diffraction model and extension for directional antennas," *Proc. IEEE 84th Veh. Technol. Conf. (VTC-Fall)*, Sep. 2016, pp. 1–6.

[58] K. Zhao, C. Gustafson, Q. Liao, S. Zhang, T. Bolin, Z. Ying, and S. He, "Channel characteristics and user body effects in an outdoor urban scenario at 15 and 28 GHz," *IEEE Trans. Antennas Propag.*, vol. 65, no. 12, pp. 6534–6548, Dec. 2017.

[59] *Qualcomm Announces First End-to-End 802.11ax Wi-Fi Portfolio | Qualcomm*, Qualcomm, San Diego, CA, USA, Mar. 2017.

[60] ASUS Press News. *ASUS presents the edge of beyond at IFA 2017*. Accessed: May 29, 2019. [Online]. Available: https://press.asus.com/

[61] Netgear. *Nighthawk X10 Smart WiFi Router*. Accessed: May 29, 2019. [Online]. Available: https://www.netgear.com/landings/ad7200/

[62] R. Wu *et al.*, "64-QAM 60-GHz CMOS transceivers for IEEE 802.11ad/ay," *IEEE J. Solid-State Circuits*, vol. 52, no. 11, pp. 2871–2891, Nov. 2017.

[63] M. Giordani and M. Zorzi, "Improved user tracking in 5G millimeter wave mobile networks via refinement operations," in *Proc. 16th Annual Mediterranean Ad Hoc Netw. Workshop (Med-Hoc-Net)*, Jun. 2017, pp. 1–8.

[64] M. Boers *et al.*, "A 16TX/16RX 60 GHz 802.11ad chipset with single coaxial interface and polarization diversity," *IEEE J. Solid-State Circuits*, vol. 49, no. 12, pp. 3031–3045, Dec. 2014.

[65] S. Emami, R. F. Wiser, E. Ali, M. G. Forbes, M. Q. Gordon, X. Guan, S. Lo, P. T. McElwee, J. Parker, J. R. Tani, J. M. Gilbert, and C. H. Doan, "A 60 GHz CMOS phased-array transceiver pair for multi-Gb/s wireless communications," in *IEEE Int. Solid-State Circuits Conf. (ISSCC) Dig. Tech. Papers*, Feb. 2011, pp. 164–165.

[66] K. Zhao, S. Zhang, Z. Ho, O. Zander, T. Bolin, Z. Ying, and G. F. Pedersen, "Spherical coverage characterization of 5G millimeter wave user equipment with 3GPP specifications," *IEEE Access*, vol. 7, pp. 4442–4452, 2019.

[67] *UE Spherical Coverage Measurements at mmWave 28 GHz*, document R4-1807490, 3GPP TSG-RAN WG4 Meeting #87, Sony, Busan, South Korea, May 2018.

[68] A. Alammouri, J. Mo, B. L. Ng, J. C. Zhang, and J. G. Andrews, "Hand grip impact on 5G mmWave mobile devices," *IEEE Access*, vol. 7, pp. 60532–60544, 2019.

[69] Y. Tousi and E. Afshari, "A high-power and scalable 2-D phased array for terahertz CMOS integrated systems," *IEEE J. Solid-State Circuits*, vol. 50, no. 2, pp. 597–609, Feb. 2015.

[70] A. S. Y. Poon and M. Taghivand, "Supporting and enabling circuits for antenna arrays in wireless communications," *Proc. IEEE*, vol. 100, no. 7, pp. 2207–2218, Jul. 2012.

[71] B. Yang, Z. Yu, J. Lan, R. Zhang, J. Zhou, and W. Hong, "Digital beamforming-based massive MIMO transceiver for 5G millimeter-wave communications," *IEEE Trans. Microw. Theory Techn.*, vol. 66, no. 7, pp. 3403–3418, Jul. 2018.

[72] Y. Cai, Z. Qin, F. Cui, G. Y. Li, and J. A. McCann, "Modulation and multiple access for 5G networks," *IEEE Commun. Surveys Tuts.*, vol. 20, no. 1, pp. 629–646, 1st Quart., 2018.

[73] O. El Ayach, S. Rajagopal, S. Abu-Surra, Z. Pi, and R. W. Heath, Jr., "Spatially sparse precoding in millimeter wave MIMO systems," *IEEE Trans. Wireless Commun.*, vol. 13, no. 3, pp. 1499–1513, Mar. 2014.

[74] A. F. Molisch, V. V. Ratnam, S. Han, Z. Li, S. Le Hong Nguyen, L. Li, and K. Haneda, "Hybrid beamforming for massive MIMO: A survey," *IEEE Commun. Mag.*, vol. 55, no. 9, pp. 134–141, Sep. 2017.

[75] L. Liang, W. Xu, and X. Dong, "Low-complexity hybrid precoding in massive multiuser MIMO systems," *IEEE Wireless Commun. Lett.*, vol. 3, no. 6, pp. 653–656, Dec. 2014.

[76] F. Sohrabi and W. Yu, "Hybrid digital and analog beamforming design for large-scale antenna arrays," *IEEE J. Sel. Topics Signal Process.*, vol. 10, no. 3, pp. 501–513, Apr. 2016.

[77] C.-X. Mao, S. Gao, and Y. Wang, "Broadband high-gain beam-scanning antenna array for millimeter-wave applications," *IEEE Trans. Antennas Propag.*, vol. 65, no. 9, pp. 4864–4868, Sep. 2017.

[78] C.-X. Mao, S. Gao, Y. Wang, Q. Luo, and Q.-X. Chu, "A shared-aperture dual-band dual-polarized filtering-antenna-array with improved frequency response," *IEEE Trans. Antennas Propag.*, vol. 65, no. 4, pp. 1836–1844, Apr. 2017.

[79] W. Zhai, V. Miraftab, M. Repeta, D. Wessel, and W. Tong, "Dual-band millimeter-wave interleaved antenna array exploiting low-cost PCB technology for high speed 5G communication," in *IEEE MTT-S Int. Microw. Symp. Dig.*, May 2016, pp. 1–3.

[80] H. M. Cheema and A. Shamim, "The last barrier: On-chip antennas," *IEEE Microw. Mag.*, vol. 18, no. 1, pp. 79–91, Jan./Feb. 2013.

[81] S. Liao and Q. Xue, "Dual polarized planar aperture antenna on LTCC for 60-GHz antenna-in-package applications," *IEEE Trans. Antennas Propag.*, vol. 65, no. 1, pp. 63–70, Jan. 2017.

[82] A. Natarajan, S. K. Reynolds, M.-D. Tsai, S. T. Nicolson, J.-H. C. Zhan, D. G. Kam, D. Liu, Y.-L. O. Huang, A. Valdes-Garcia, and B. A. Floyd, "A fully-integrated 16-element phased-array receiver in SiGe BiCMOS for 60-GHz communications," *IEEE J. Solid-State Circuits*, vol. 46, no. 5, pp. 1059–1075, May 2011.

[83] S. Li, T. Chi, J. Park, W. Khan, H. Wang, and J. Papapolymerou, "A fully packaged D-band MIMO transmitter using high-density flip-chip interconnects on LCP substrate," in *IEEE MTT-S Int. Microw. Symp. Dig.*, May 2016, pp. 1–4.

[84] T. Deckmyn, S. Agneessens, A. C. F. Reniers, A. B. Smolders, M. Cauwe, D. V. Ginste, and H. Rogier, "A novel 60 GHz wideband coupled half-mode/quarter-mode substrate integrated waveguide antenna," *IEEE Trans. Antennas Propag.*, vol. 65, no. 12, pp. 6915–6926, Dec. 2017.

[85] X.-Y. Bao, Y.-X. Guo, and Y.-Z. Xiong, "60-GHz AMC-based circularly polarized on-chip antenna using standard 0.18-μm CMOS technology," *IEEE Trans. Antennas Propag.*, vol. 60, no. 5, pp. 2234–2241, May 2012.

[86] Y. Huo, X. Dong, and J. Bornemann, "A wideband artificial magnetic conductor yagi antenna for 60-GHz standard 0.13-μm CMOS applications," in *Proc. 12th IEEE Int. Conf. Solid-State Integr. Circuit Technol. (ICSICT)*, Guilin, China, Oct. 2014, pp. 1–3.

[87] H. T. Huang, B. Yuan, Z. F. Hu, G. Q. Luo, and X. H. Zhang, "A circular ring-shape monopole on-chip antenna with artificial magnetic conductor," *Proc. Asia–Pacific Microw. Conf. (APMC)*, Dec. 2015, pp. 1–3.

[88] L. Jing, C. R. Rowell, S. Raju, M. Chan, R. D. Murch, and C. P. Yue, "Fabrication and measurement of millimeter-wave on-chip MIMO antenna for CMOS RFIC's," in *Proc. MTT-S IEEE Int. Wireless Symp. (IWS)*, Mar. 2016, pp. 1–4.

[89] H. Wang, F. Wang, H. T. Nguyen, S. Li, T.-Y. Huang, A. S. Ahmed, M. E. D. Smith, N. S. Mannem, and J. Lee. *Power Amplifiers Performance Survey 2000-Present*. Accessed: May 29, 2019. [Online]. Available: https://gems.ece.gatech.edu/PA_survey.html

[90] *Report and Order and Future Notice of Proposed Rulemaking*. Accessed: May 29, 2019. [Online]. Available: https://apps.fcc.gov/edocs_public/attachmatch/FCC-16-89A1.pdf

[91] C. Li, M. Wang, T. Chi, A. Kumar, M. Boenke, N. Cahoon, A. Bandyopadhyay, A. Joseph, and H. Wang, "A high-efficiency 5G K/Ka-band stacked power amplifier in 45 nm CMOS SOI process supporting 9 Gb/s 64-QAM modulation with 22.4% average PAE," in *Proc. Texas Symp. IEEE Wireless Microw. Circuits Syst. (WMCS)*, Mar. 2017, pp. 1–4.

[92] S. R. Helmi, J.-H. Chen, and S. Mohammadi, "High-efficiency microwave and mm-wave stacked cell CMOS SOI power amplifiers," *IEEE Trans. Microw. Theory Techn.*, vol. 64, no. 7, pp. 2025–2038, Jul. 2016.

[93] T. Li and H. Wang, "A continuous-mode 23.5–41 GHz hybrid Class-F/F-1 power amplifier with 46% peak PAE for 5G massive MIMO applications," in *Proc. IEEE Radio Freq. Integr. Circuits Symp. (RFIC)*, Philadelphia, PA, USA, Jun. 2018, pp. 220–230.

[94] H. T. Nguyen, T. Chi, S. Li, and H. Wang, "A 62-to-68 GHz linear 6 Gb/s 64 QAM CMOS Doherty radiator with 27.5%/20.1% PAE at peak/6 dB-back-off output power leveraging high-efficiency multi-feed antenna-based active load modulation," in *IEEE Int. Solid-State Circuits Conf. (ISSCC) Dig. Tech. Papers*, San Francisco, CA, USA, Feb. 2018, pp. 402–404.

[95] Y. Beltagy, P. Mitran, and S. Boumaiza, "Direct learning algorithm for digital predistortion training using sub-Nyquist intermediate frequency feedback signal," *IEEE Trans. Microw. Theory Techn.*, vol. 67, no. 1, pp. 267–277, Jan. 2019.

[96] K. Gumber and M. Rawat, "A modified hybrid RF predistorter linearizer for ultra wideband 5G systems," *IEEE J. Emerg. Sel. Topics Circuits Syst.*, vol. 7, no. 4, pp. 547–557, Dec. 2017.

[97] S.-H. Li, S. S. H. Hsu, J. Zhang, and K.-C. Huang, "Design of a compact GaN MMIC Doherty power amplifier and system level analysis with X-parameters for 5G communications," *IEEE Trans. Microw. Theory Techn.*, vol. 66, no. 12, pp. 5676–5684, Dec. 2018.

[98] G. Liu and H. Schumacher, "Broadband millimeter-wave LNAs (47–77 GHz and 70–140 GHz) using a T-type matching topology," *IEEE J. Solid-State Circuits*, vol. 48, no. 9, pp. 2022–2029, Sep. 2013.

[99] Y. Yu, H. Liu, Y. Wu, and K. Kang, "A 54.4-90 GHz low-noise amplifier in 65-nm CMOS," *IEEE J. Solid-State Circuits*, vol. 52, no. 11, pp. 2892–2904, Nov. 2017.

[100] U. Kodak and G. M. Rebeiz, "A 5G 28-GHz common-leg T/R front-end in 45-nm CMOS SOI with 3.7-dB NF and −30-dBc EVM with 64-QAM/500-MBaud modulation," *IEEE Trans. Microw. Theory Techn.*, vol. 67, no. 1, pp. 318–331, Jan. 2019.

[101] V. Chauhan and B. Floyd, "A 24–44 GHz UWB LNA for 5G cellular frequency bands," in *Proc. 11th Global Symp. Millim. Waves (GSMM)*, Boulder, CO, USA, 2018, pp. 1–3.

[102] W. Wang, H. Yin, X. Chen, and W. Wang, "Hybrid beamforming design and performance with imperfect phase shifters in multiuser millimeter wave systems," 2018, *arXiv:1803.00317*. [Online]. Available: https://arxiv.org/abs/1803.00317

[103] M. Sato, T. Takahashi, and T. Hirose, "68–110-GHz-band low-noise amplifier using current reuse topology," *IEEE Trans. Microw. Theory Techn.*, vol. 58, no. 7, pp. 1910–1916, Jul. 2010.

[104] Y. Yu, P. Baltus, A. van Roermund, D. Jeurissen, A. de Graauw, E. van der Heijden, and R. Pijper, "A 60 GHz digitally controlled phase shifter in CMOS," in *IEEE Int. Solid-State Circuits Conf. (ISSCC) Dig. Tech. Papers*, Sep. 2008, pp. 250–253.

[105] M.-D. Tsai and A. Natarajan, "60 GHz passive and active RF-path phase shifters in silicon," in *Proc. IEEE Radio Freq. Integr. Circuits Symp.*, Boston, MA, USA, Jun. 2009, pp. 223–226.

[106] E. Cohen, C. Jakobson, S. Ravid, and D. Ritter, "A bidirectional TX/RX four-element phased array at 60 GHz with RF-IF conversion block in 90-nm CMOS process," *IEEE Trans. Microw. Theory Techn.*, vol. 58, no. 5, pp. 1438–1446, May 2010.

[107] D. Pepe and D. Zito, "Two mm-wave vector modulator active phase shifters with novel IQ generator in 28 nm FDSOI CMOS," *IEEE J. Solid-State Circuits*, vol. 52, no. 2, pp. 344–356, Feb. 2017.

[108] J. Pang, R. Kubozoe, Z. Li, M. Kawabuchi, and K. Okada, "A 28 GHz CMOS phase shifter supporting 11.2 Gb/s in 256 QAM with an RMS gain error of 0.13 dB for 5G mobile network," in *Proc. 48th Eur. Microw. Conf. (EuMC)*, Madrid, Spain, 2018, pp. 807–810.

[109] W.-T. Li, Y.-C. Chiang, J.-H. Tsai, H.-Y. Yang, J.-H. Cheng, and T.-W. Huang, "60-GHz 5-bit phase shifter with integrated VGA phase-error compensation," *IEEE Trans. Microw. Theory Techn.*, vol. 61, no. 3, pp. 1224–1235, Mar. 2013.

[110] Y. Tousi and A. Valdes-Garcia, "A Ka-band digitally-controlled phase shifter with sub-degree phase precision," in *Proc. IEEE RFIC Symp. Dig. Papers*, May 2016, pp. 356–359.

[111] Y.-S. Yeh, B. Walker, E. Balboni, and B. A. Floyd, "A 28-GHz 4-channel dual-vector receiver phased array in SiGe BiCMOS technology," in *Proc. IEEE Radio Freq. Integr. Circuits Symp. (RFIC)*, San Francisco, CA, USA, May 2016, pp. 352–355.

[112] K.-J. Koh and G. M. Rebeiz, "0.13-μm CMOS phase shifters for X-, Ku-, and K-band phased arrays," *IEEE J. Solid-State Circuits*, vol. 42, no. 11, pp. 2535–2546, Nov. 2007.

[113] Y. Yu, P. G. M. Baltus, A. De Graauw, E. van der Heijden, C. S. Vaucher, and A. H. M. van Roermund, "A 60 GHz phase shifter integrated with LNA and PA in 65 nm CMOS for phased array systems," *IEEE J. Solid-State Circuits*, vol. 45, no. 9, pp. 1697–1709, Sep. 2010.

[114] A. D. Berny, A. M. Niknejad, and R. G. Meyer, "A 1.8-GHz LC VCO with 1.3-GHz tuning range and digital amplitude calibration," *IEEE J. Solid-State Circuits*, vol. 40, no. 4, pp. 909–917, Apr. 2005.

[115] P. Andreani, K. Kozmin, P. Sandrup, M. Nilsson, and T. Mattsson, "A TX VCO for WCDMA/EDGE in 90 nm RF CMOS," *IEEE J. Solid-State Circuits*, vol. 46, no. 7, pp. 1618–1626, Jul. 2011.

[116] Y. Huo, T. Mattsson, and P. Andreani, "A switched-transformer, 76% tuning-range VCO in 90 nm CMOS," in *Proc. Asia–Pacific Microw. Conf. (APMC)*, Dec. 2010, pp. 1043–1046.

[117] A. Liscidini, L. Fanori, P. Andreani, and R. Castello, "A power-scalable DCO for multi-standard GSM/WCDMA frequency synthesizers," *IEEE J. Solid-State Circuits*, vol. 49, no. 3, pp. 646–656, Mar. 2014.

[118] Y. Huo, X. Dong, L. Li, M. Xie, and W. Xu, "26/40 GHz CMOS VCOs design of radio front-end for 5G mobile devices," in *Proc. IEEE Int. Conf. Ubiquitous Wireless Broadband (ICUWB)*, Oct. 2016, pp. 1–4.

[119] B. Catli and M. M. Hella, "Triple-push operation for combined oscillation/divison functionality in millimeter-wave frequency synthesizers," *IEEE J. Solid-State Circuits*, vol. 45, no. 8, pp. 1575–1589, Aug. 2010.

[120] Z. Zong, M. Babaie, and R. B. Staszewski, "A 60 GHz frequency generator based on a 20 GHz oscillator and an implicit multiplier," *IEEE J. Solid-State Circuits*, vol. 51, no. 5, pp. 1261–1273, May 2016.

[121] W. Deng, T. Siriburanon, A. Musa, K. Okada, and A. Matsuzawa, "A sub-harmonic injection-locked quadrature frequency synthesizer with frequency calibration scheme for millimeter-wave TDD transceivers," *IEEE J. Solid-State Circuits*, vol. 48, no. 7, pp. 1710–1720, Jul. 2013.

[122] H. Yoon, J. Kim, S. Park, Y. Lim, Y. Lee, J. Bang, K. Lim, and J. Choi, "A −31 dBc integrated-phase-noise 29GHz fractional-N frequency synthesizer supporting multiple frequency bands for backward-compatible 5G using a frequency doubler and injection-locked frequency multipliers," in *IEEE Int. Solid-State Circuits Conf. (ISSCC) Dig. Tech. Papers*, Feb. 2018, pp. 366–368.

[123] F. Piri, M. Bassi, N. R. Lacaita, A. Mazzanti, and F. Svelto, "A PVT-tolerant >40-dB IRR, 44% fractional-bandwidth ultra-wideband mm-wave quadrature LO generator for 5G networks in 55-nm CMOS," *IEEE J. Solid-State Circuits*, vol. 53, no. 12, pp. 3576–3586, Dec. 2018.

[124] M. Xiao, S. Mumtaz, Y. Huang, L. Dai, Y. Li, M. Matthaiou, G. K. Karagiannidis, E. Björnson, K. Yang, C.-L. I, and A. Ghosh, "Millimeter wave communications for future mobile networks," *IEEE J. Sel. Areas Commun.*, vol. 35, no. 9, pp. 1909–1935, Sep. 2017.

[125] A. Alkhateeb, O. El Ayach, G. Leus, and R. W. Heath, Jr., "Channel estimation and hybrid precoding for millimeter wave cellular systems," *IEEE J. Sel. Topics Signal Process.*, vol. 8, no. 5, pp. 831–846, Oct. 2014.

[126] Y. Zhang, Y. Huo, D. Wang, X. Dong, and X. You, "Channel estimation and hybrid precoding for distributed phased arrays based MIMO wireless communications," 2019, *arXiv:1903.05928*. [Online]. Available: https://arxiv.org/abs/1903.05928

[127] J. Wang, Z. Lan, C.-W. Pyo, T. Baykas, C.-S. Sum, M. A. Rahman, J. Gao, R. Funada, F. Kojima, H. Harada, and S. Kato, "Beam codebook based beamforming protocol for multi-Gbps millimeter-wave WPAN systems," *IEEE J. Sel. Areas Commun.*, vol. 27, no. 8, pp. 1390–1399, Oct. 2009.

[128] *WiGiG MAC and PHY Specification, Version 1.2*, Wireless Gigabit Alliance, Inc., Austin, TX, USA, Mar. 2013.

[129] K. Hosoya, N. Prasad, K. Ramachandran, N. Orihashi, S. Kishimoto, S. Rangarajan, and K. Maruhashi, "Multiple sector ID capture (MIDC): A novel beamforming technique for 60-GHz band multi-Gbps WLAN/PAN systems," *IEEE Trans. Antennas Propag.*, vol. 63, no. 1, pp. 81–96, Jan. 2015.

[130] J. Zhang, Y. Huang, Q. Shi, J. Wang, and L. Yang, "Codebook design for beam alignment in millimeter wave communication systems," *IEEE Trans. Commun.*, vol. 65, no. 11, pp. 4980–4995, Nov. 2017.

[131] X. Gao, L. Dai, C. Yuen, and Z. Wang, "Turbo-like beamforming based on tabu search algorithm for millimeter-wave massive MIMO systems," *IEEE Trans. Veh. Technol.*, vol. 65, no. 7, pp. 5731–5737, Jul. 2016.

[132] X. Gao, L. Dai, Y. Sun, S. Han, and I. Chih-Lin, "Machine learning inspired energy-efficient hybrid precoding for mmWave massive MIMO systems," in *Proc. IEEE Int. Conf. Commun. (ICC)*, Paris, France, May 2017, pp. 1–6.

[133] A. Alkhateeb, S. Alex, P. Varkey, Y. Li, Q. Qu, and D. Tujkovic, "Deep learning coordinated beamforming for highly-mobile millimeter wave systems," *IEEE Access*, vol. 6, pp. 37328–37348, 2018.

[134] Y. Sun, Z. Gao, H. Wang, and D. Wu, "Machine learning based hybrid precoding for mmWave MIMO-OFDM with dynamic subarray," in *Proc. IEEE Globecom Workshops (GC Wkshps)*, Abu Dhabi, United Arab Emirates, Sep. 2018, pp. 1–6.

[135] Y. Wang, M. Narasimha, and R. W. Heath, Jr., "MmWave beam prediction with situational awareness: A machine learning approach," in *Proc. IEEE 19th Int. Workshop Signal Process. Adv. Wireless Commun. (SPAWC)*, Kalamata, Greece, Jun. 2018, pp. 1–5.

[136] Z. Xiao, T. He, P. Xia, and X.-G. Xia, "Hierarchical codebook design for beamforming training in millimeter-wave communication," *IEEE Trans. Wireless Commun.*, vol. 15, no. 5, pp. 3380–3392, May 2016.

[137] Y. Sun, Z. Gao, H. Wang, B. Shim, G. Gui, G. Mao, and F. Adachi, "Principal component analysis based broadband hybrid precoding for millimeter-wave massive MIMO systems," 2019, *arXiv:1903.09074*. [Online]. Available: https://arxiv.org/abs/1903.09074

[138] L. V. der Perre, L. Liu, and E. G. Larsson, "Efficient DSP and circuit architectures for Massive MIMO: State of the art and future directions," *IEEE Trans. Signal Process.*, vol. 66, no. 18, pp. 4717–4736, Sep. 2018.

[139] S. Malkowsky, J. Vieira, K. Nieman, N. Kundargi, I. Wong, V. Öwall, O. Edfors, F. Tufvesson, and L. Liu, "Implementation of low-latency signal processing and data shuffling for TDD Massive MIMO systems," *Proc. IEEE Int. Workshop Signal Process. Syst.*, Dec. 2016, pp. 260–265.

[140] V. Raghavan, J. Cezanne, S. Subramanian, A. Sampath, and O. Koymen, "Beamforming tradeoffs for initial UE discovery in millimeter-wave MIMO systems," *IEEE J. Sel. Topics Signal Process.*, vol. 10, no. 3, pp. 543–559, Apr. 2016.

[141] Y.-Y. Lee, C.-H. Wang, and Y.-H. Huang, "A hybrid RF/baseband precoding processor based on parallel-index-selection matrix-inversion-bypass simultaneous orthogonal matching pursuit for millimeter wave MIMO systems," *IEEE Trans. Signal Process.*, vol. 63, no. 2, pp. 305–317, Jan. 2015.

[142] H. Prabhu, J. N. Rodrigues, L. Liu, and O. Edfors, "A 60 pJ/b 300 Mb/s 128 × 8 Massive MIMO precoder-detector in 28 nm FD-SOI," in *IEEE Int. Solid-State Circuits Conf. (ISSCC) Dig. Tech. Papers*, Feb. 2017, pp. 60–61.

[143] W. Tang, H. Prabhu, L. Liu, V. Öwall and Z. Zhang, "A 1.8 Gb/s 70.6 pJ/b 128 × 16 link-adaptive near-optimal massive MIMO detector in 28 nm UTBB-FDSOI," in *IEEE Int. Solid-State Circuits Conf. (ISSCC) Dig. Tech. Papers*, Feb. 2018, pp. 224–226.

[144] S. Han, Y.-C. Liang, Q. Chen, and B.-H. Soong, "Licensed-assisted access for LTE in unlicensed spectrum: A MAC protocol design," *IEEE J. Sel. Areas Commun.*, vol. 34, no. 10, pp. 2550–2561, Oct. 2016.

[145] K. Thilina, K. W. Choi, N. Saquib, and E. Hossain, "Machine learning techniques for cooperative spectrum sensing in cognitive radio networks," *IEEE J. Sel. Areas Commun.*, vol. 31, no. 11, pp. 2209–2221, Nov. 2013.

[146] M. Pesce. *Meet the Mate 10, Huawei's New AI-Powered Flagship Phone*. Accessed: May 29, 2019. [Online]. Available: https://www.wired.com/story/huawei-mate-10-and-mate-10-pro/

[147] O. Shacham. *Pixel Visual Core: Image Processing and Machine Learning on Pixel 2*. Accessed: May 29, 2019. [Online]. Available: https://www.blog.google/products/pixel/pixel-visual-core-image-processing-and-machine-learning-pixel-2/

[148] Apple. *Apple Special Event. September 12, 2017. The First-Ever Event at the Steve Jobs Theater*. Accessed: May 29, 2019. [Online]. Available: https://www.apple.com/apple-events/september-2017/

[149] Computer Vision Machine Learning Team, "An on-device deep neural network for face detection," *Apple Mach. Learn. J.*, vol. 1, no. 7, Nov. 2017. [Online]. Available: https://machinelearning.apple.com/2017/11/16/face-detection.html

[150] H. Ye, G. Y. Li, and B.-H. Juang, "Power of deep learning for channel estimation and signal detection in OFDM systems," *IEEE Wireless Commun. Lett.*, vol. 7, no. 1, pp. 114–117, Feb. 2018.

[151] X. Wang, L. Gao, S. Mao, and S. Pandey, "CSI-based fingerprinting for indoor localization: A deep learning approach," *IEEE Trans. Veh. Technol.*, vol. 66, no. 1, pp. 763–776, Jan. 2017.

[152] M. T. Hoang, Y. Zhu, B. Yuen, T. Reese, X. Dong, T. Lu, R. Westendorp, and M. Xie, "A soft range limited K-nearest neighbors algorithm for indoor localization enhancement," *IEEE Sensors J.*, vol. 18, no. 24, pp. 10208–10216, Dec. 2018.

[153] A. Silver, "IEEE Spectrum's general technology blog, featuring news, analysis, and opinions about engineering, consumer electronics, and technology and society, from the editorial staff and freelance contributors," *IEEE Spectr.*, Jun. 2018. [Online]. Available: https://spectrum.ieee.org/blog/tech-talk

[154] L. Zhang, Q. Gao, X. Ma, J. Wang, T. Yang, and H. Wang, "DeFi: Robust training-free device-free wireless localization with WiFi," *IEEE Trans. Veh. Technol.*, vol. 67, no. 9, pp. 8822–8831, Sep. 2018.

[155] F. Adib and D. Katabi, "See through walls with WiFi! " *Proc. ACM SIGCOMM. ACM*, 2013, pp. 75–86.

[156] Y. Wang, K. Wu, and L. M. Ni, "WiFall: Device-free fall detection by wireless networks," *IEEE Trans. Mobile Comput.*, vol. 16, no. 2, pp. 581–594, Feb. 2017.

[157] Y.-L. Ban, C. Li, C.-Y.-D. Sim, G. Wu, and K.-L. Wong, "4G/5G multiple antennas for future multi-mode smartphone applications," *IEEE Access*, vol. 4, pp. 2981–2988, 2016.

[158] Y. Wang and Z. Du, "A wideband printed dual-antenna with three neutralization lines for mobile terminals," *IEEE Trans. Antennas Propag.*, vol. 62, no. 3, pp. 1495–1500, Mar. 2014.

[159] H. Xu, H. Zhou, S. Gao, H. Wang, and Y. Cheng, "Multimode decoupling technique with independent tuning characteristic for mobile," *IEEE Trans. Antennas Propag.*, vol. 65, no. 12, pp. 6739–6751, Dec. 2017.

[160] *Wireless Power Consortium*. Accessed: May 29, 2019. [Online]. Available: http://www. wirelesspowerconsortium.com/

[161] X. Lu, P. Wang, D. Niyato, D. I. Kim, and Z. Han, "Wireless charging technologies: Fundamentals, standards, and network applications," *IEEE Commun. Surveys Tuts.*, vol. 18, no. 2, pp. 1413–1452, 2nd Quart., 2016.

[162] S. Y. Hui, "Planar wireless charging technology for portable electronic products and Qi," *Proc. IEEE*, vol. 101, no. 6, pp. 1290–1301, Jun. 2013.

[163] B. Yu, K. Yang, C.-Y.-D. Sim, and G. Yang, "A novel 28 GHz beam steering array for 5G mobile device with metallic casing application," *IEEE Trans. Antennas Propag.*, vol. 66, no. 1, pp. 462–466, Jan. 2018.

[164] B. Xu, Z. Ying, L. Scialacqua, A. Scannavini, L. J. Foged, T. Bolin, K. Zhao, S. He, and M. Gustafsson, "Radiation performance analysis of 28 GHz antennas integrated in 5G mobile terminal housing," *IEEE Access*, vol. 6, pp. 48088–48101, 2018.

[165] *Xiaomi Mi MIX*. Accessed: May 29, 2019. [Online]. Available: http://www.mi.com/en/mix/specs/

[166] T. S. Rappaport, Y. Xing, G. R. MacCartney, A. F. Molisch, E. Mellios, and J. Zhang, "Overview of millimeter wave communications for fifth-generation (5G) wireless networks—With a focus on propagation models," *IEEE Trans. Antennas Propag.*, vol. 65, no. 12, pp. 6213–6230, Dec. 2017.

[167] *Samsung*. Accessed: May 29, 2019. [Online]. Available: https://www.samsung.com/ca/pre-registration/

[168] *Huawei*. Accessed: May 29, 2019. [Online]. Available: https://consumer.huawei.com/ca/phones/ mate-x/

[169] H. Chen, J. He, and S.-T. Wu, "Recent advances on quantum-dot-enhanced liquid-crystal displays," *IEEE J. Sel. Topics Quantum Electron.*, vol. 23, no. 5, pp. 1–11, Jan. 2017.

[170] A. Nordrum, "Fold-up screens could make their big debut [top tech 2017]," *IEEE Spectr.*, vol. 54, no. 1, pp. 50–51, Jan. 2017.

[171] A. Kunert, T. Weissker, B. Froehlich, and A. Kulik, "Multi-window 3D interaction for collaborative virtual reality," *IEEE Trans. Vis. Comput. Graphics*, to be published.

[172] B. Hoppenstedt, T. Probst, M. Reichert, W. Schlee, K. Kammerer, M. Spiliopoulou, J. Schobel, M. Zimoch, A. Felnhofer, O. Kothgassner, and R. Pryss, "Applicability of immersive analytics in mixed reality: Usability study," *IEEE Access*, vol. 7, pp. 71921–71932, 2019.

[173] K. Ajito and Y. Ueno, "THz chemical imaging for biological applications," *IEEE Trans. THz Sci. Technol.*, vol. 1, no. 1, pp. 293–300, Sep. 2011.

[174] A. Tang, T. Reck, and G. Chattopadhyay, "CMOS system-on-chip techniques in millimeter-wave/THz instruments and communications for planetary exploration," *IEEE Commun. Mag.*, vol. 54, no. 10, pp. 176–182, Oct. 2016.

[175] C. Wang, B. Perkins, Z. Wang, and R. Han, "Molecular detection for unconcentrated gas with ppm sensitivity using 220-to-320-GHz dual-frequency-comb spectrometer in CMOS," *IEEE Trans. Biomed. Circuits Syst.*, vol. 12, no. 3, pp. 709–721, Jun. 2018.

[176] C. Kulesa, "Terahertz spectroscopy for astronomy: From comets to cosmology," *IEEE Trans. THz Sci. Technol.*, vol. 1, no. 1, pp. 232–240, Sep. 2011.

[177] C. Wang, X. Yi, J. Mawdsley, M. Kim, Z. Wang, and R. Han, "An on-chip fully electronic molecular clock based on sub-terahertz rotational spectroscopy," *Nature Electron.*, vol. 1, no. 7, pp. 421–427, 2018.

[178] X. Lin, Y. Rivenson, N. T. Yardimci, M. Veli, Y. Luo, M. Jarrahi, and A. Ozcan, "All-optical machine learning using diffractive deep neural networks," *Science*, vol. 361, no. 6406, pp. 1004–1008, Sep. 2018.

[179] Q. J. Gu, "THz interconnect: The last centimeter communication," *IEEE Commun. Mag.*, vol. 53, no. 4, pp. 206–215, Apr. 2015.

[180] H.-J. Song and T. Nagatsuma, "Present and future of terahertz communications," *IEEE Trans. Terahertz Sci. Technol.*, vol. 1, no. 1, pp. 256–263, Sep. 2011.

[181] *Attenuation Due to Clouds and Fog*, document ITU Recommendation ITU-R P.676-11, Sep. 2016. [Online]. Available: https://www.itu.int/rec/R-REC-P.676/en

[182] B. Heinemann, "SiGe HBT with f_T/f_{max} of 505 GHz/720 GHz," in *IEDM Tech. Dig.*, San Francisco, CA, USA, Dec. 2016, pp. 3.1.1–3.1.4.

[183] M. H. Eissa, A. Malignaggi, R. Wang, M. Elkhouly, K. Schmalz, A. C. Ulusoy, and D. Kissinger, "Wideband 240-GHz transmitter and receiver in BiCMOS technology with 25-Gbit/s data rate," *IEEE J. Solid-State Circuits*, vol. 53, no. 9, pp. 2532–2542, Sep. 2018.

[184] A. Tang, G. Virbila, D. Murphy, F. Hsiao, Y.-H. Wang, Q. J. Gu, Z. Xu, Y. Wu, M. Zhu, and M.-C. F. Chang, "A 144 GHz 0.76 cm-resolution sub-carrier SAR phase radar for 3D imaging in 65 nm CMOS," in *IEEE Int. Solid-State Circuits Conf. (ISSCC) Dig. Tech. Papers*, San Francisco, CA, USA, Feb. 2012, pp. 264–266.

[185] R. A. Hadi, H. Sherry, J. Grzyb, Y. Zhao, W. Forster, H. M. Keller, A. Cathelin, A. Kaiser, and U. R. Pfeiffer, "A 1 k-pixel video camera for 0.7–1.1 terahertz imaging applications in 65-nm CMOS," *IEEE J. Solid-State Circuits*, vol. 47, no. 12, pp. 2999–3012, Dec. 2012.

[186] Y. Kim, Y. Zhang, T. J. Reck, D. J. Nemchick, G. Chattopadhyay, B. Drouin, M.-C. F. Chang, and A. Tang, "A 183-GHz InP/CMOS-hybrid heterodyne-spectrometer for spaceborne atmospheric remote sensing," *IEEE Trans. THz Sci. Technol.*, vol. 9, no. 3, pp. 313–334, May 2019.

[187] A. Standaert and P. Reynaert, "A 400-GHz 28-nm TX and RX with chip-to-waveguide transitions used in fully integrated lensless imaging system," *IEEE Trans. THz Sci. Technol.*, vol. 9, no. 4, pp. 373–382, Jul. 2019.

[188] U. R. Pfeiffer, Y. Zhao, J. Grzyb, R. A. Hadi, N. Sarmah, W. Förster, H. Rücker, and B. Heinemann, "A 0.53 THz reconfigurable source module with up to 1 mW radiated power for diffuse illumination in terahertz imaging applications," *IEEE J. Solid-State Circuits*, vol. 49, no. 12, pp. 2938–2950, Dec. 2014.

[189] T. S. Rappaport, Y. Xing, S. Ju, and O. Kanhere, "Wireless communications and applications above 100 GHz: Opportunities and challenges for 6G and beyond," *IEEE Access*, vol. 7, pp. 78729–78757, Feb. 2019. [Online]. Available: https://wireless.engineering.nyu.edu/wireless-communication-and-applications-above-100-ghz-opportunities-and-challenges-for-6g-beyond/

[190] H. Hamada, T. Fujimura, I. Abdo, K. Okada, H.-J. Song, H. Sugiyama, H. Matsuzaki, and H. Nosaka, "300-GHz. 100-Gb/s InP-HEMT wireless transceiver using a 300-GHz fundamental mixer," in *IEEE MTT-S Int. Microw. Symp. Dig.*, Jun. 2018, pp. 1480–1483.

[191] S. Lee, R. Dong, T. Yoshida, S. Amakawa, S. Hara, A. Kasamatsu, J. Sato, and M. Fujishima, "9.5 An 80 Gb/s 300 GHz-band single-chip CMOS transceiver," in *IEEE Int. Solid-State Circuits Conf. (ISSCC) Dig. Tech. Papers*, San Francisco, CA, USA, vol. 2019, pp. 170–172.

[192] Y. Yang, O. D. Gurbuz, and G. M. Rebeiz, "An eight-element 370–410-GHz phased-array transmitter in 45-nm CMOS SOI with peak EIRP of 8–8.5 dBm," *IEEE Trans. Microw. Theory Techn.*, vol. 64, no. 12, pp. 4241–4249, Dec. 2016.

[193] H. Zhu, N. Li, J. Zeng, X. Li, and B. Ai, "A novel 0.22-THz on-chip antenna based AMCs," in *Proc. Asia–Pacific Microw. Conf.*, Sendai, Japan, Nov. 2014, pp. 366–368.
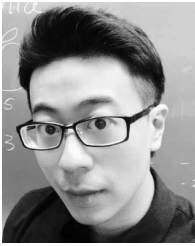
YIMING HUO (S'08–M'18) received the B.Eng. degree in information engineering from Southeast University, China, in 2006, the M.Sc. degree in system-on-chip (SoC) from Lund University, Sweden, in 2010, and the Ph.D. degree in electrical engineering from the University of Victoria, Canada, in 2017.

He has worked in several companies and institutes, including Ericsson, ST-Ericsson, the Chinese Academy of Sciences, STMicroelectronics, and Apple Inc., Cupertino, CA, USA. He is currently a Postdoctoral Research Fellow with the University of Victoria. His current research interests include 5G and beyond wireless systems, the Internet of Things, and machine learning. He is a member of several IEEE societies. He is also a member of the Massive MIMO Working Group of the IEEE Beyond 5G Roadmap. He was a recipient of the Best Student Paper Award of the 2016 IEEE ICUWB, the Excellent Student Paper Award of the 2014 IEEE ICSICT, and the Bronze Leaf Certificate of the 2010 IEEE PrimeAsia. He also received the ISSCC-STGA Award from the IEEE Solid-State Circuits Society (SSCS), in 2017. He has served as the Program Committee of the IEEE ICUWB 2017, the TPC of the IEEE VTC 2018/2019, the IEEE ICC 2019, the Session Chair of the IEEE 5G World Forum 2018, the Publication Chair of the IEEE PACRIM 2019, the Technical Reviewer for multiple premier IEEE conferences and journals.

WEI XU (S'07–M'09–SM'15) received the B.Sc. degree in electrical engineering and the M.S. and Ph.D. degrees in communication and information engineering from Southeast University, Nanjing, China, in 2003, 2006, and 2009, respectively.

From 2009 to 2010, he was a Postdoctoral Research Fellow with the Department of Electrical and Computer Engineering, University of Victoria, Canada. He is currently a Professor with the National Mobile Communications Research Laboratory, Southeast University. He has coauthored over 80 refereed journal papers in addition to 28 granted domestic patents. He holds three U.S. patents. His research interests include cooperative communications, information theory, signal processing, and machine learning for wireless communications. He received the Best Paper Awards from the IEEE MAPE, in 2013, the IEEE/CIC ICCC, in 2014, the IEEE GLOBECOM, in 2014, the IEEE ICUWB, in 2016, and WCSP, in 2017. He was a corecipient of the First Prize of the Science and Technology Award, Jiangsu, China, in 2014. He has been involved in technical program committees for international conferences, including the IEEE GLOBECOM, the IEEE ICC, the IEEE WCNC, the IEEE VTC, and the IEEE PIMRC. He was an Editor of the IEEE Communications Letters, from 2012 to 2017. He is currently an Editor of the IEEE Transactions on Communications and IEEE Access.

XIAODAI DONG (S'97–M'00–SM'09) received the B.Sc. degree in information and control engineering from Xi'an Jiaotong University, China, in 1992, the M.Sc. degree in electrical engineering from the National University of Singapore, in 1995, and the Ph.D. degree in electrical and computer engineering from Queen's University, Kingston, ON, Canada, in 2000.

From 1999 to 2002, she was with Nortel Networks, Ottawa, ON, Canada, and worked on the base transceiver design of the third-generation mobile communication systems. From 2002 to 2004, she was an Assistant Professor with the Department of Electrical and Computer Engineering, University of Alberta, Edmonton, AB, Canada. She was the Canada Research Chair (Tier II), from 2005 to 2015. Since 2005, she has been with the University of Victoria, Victoria, Canada, where she is currently a Professor with the Department of Electrical and Computer Engineering. Her research interests include 5G, mmWave communications, radio propagation, the Internet of Things, machine learning, localization, wireless security, e-health, smart grid, and nano-communications. She served as an Editor for the IEEE Transactions on Communications, from 2001 to 2007, and the IEEE Transactions on Wireless Communications, from 2009 to 2014. She is an Editor of the IEEE Transactions on Vehicular Technology.

MARVIN YUEN (S'09–M'13) received the B.Sc. degree in electrical and computer engineering from Johns Hopkins University, Baltimore, MD, USA, and the M.S. degree in electrical engineering from the Viterbi School of Engineering, University of Southern California, Los Angeles, CA, USA. He was a Patent Examiner with USPTO, Alexandria, VA, USA. He is currently a System Application Engineer with Kingston Technology.

● ● ●